JGR Atmospheres

Key Points:
- The properties of liquid Southern Ocean (SO) clouds vary with latitude
- SO low clouds are susceptible to aerosol concentrations
- SO clouds near Antarctica have high droplet numbers compared to lower latitude SO clouds

Correspondence to:
G. G. Mace,
jay.mace@utah.edu

Southern Ocean Cloud Properties Derived From CAPRICORN and MARCUS Data

Gerald G. Mace[1] , Alain Protat[2,3] , Ruhi S. Humphries[4,3] , Simon P. Alexander[5,3] , Ian M. McRobert[6] , Jason Ward[7], Paul Selleck[4], Melita Keywood[4], and Greg M. McFarquhar[8]

[1]Department of Atmospheric Sciences, University of Utah, Salt Lake City, UT, USA, [2]Australian Bureau of Meteorology, Melbourne, VIC, Australia, [3]Australian Antarctic Partnership Program, Institute for Marine and Antarctic Studies, University of Tasmania, Hobart, TAS, Australia, [4]Climate Science Centre, CSIRO Oceans and Atmosphere, Aspendale, VIC, Australia, [5]Australian Antarctic Division, Kingston, TAS, Australia, [6]Engineering and Technology Program, CSIRO Oceans and Atmosphere, Hobart, TAS, Australia, [7]Climate Science Center/Atmospheric Composition and Chemistry/Aerosols, Oceans and Atmosphere, CSIRO, Aspendale, VIC, Australia, [8]Cooperative Institute for Mesoscale Meteorological Studies (CIMMS) and School of Meteorology, University of Oklahoma, Norman, OK, USA

Abstract The properties of Southern Ocean (SO) liquid phase non precipitating clouds (hereafter clouds) are examined using shipborne data collected during the Measurements of Aerosols, Radiation and Clouds over the Southern Ocean and the Clouds Aerosols Precipitation Radiation and atmospheric Composition Over the SoutheRN ocean I and II campaigns that took place south of Australia during Autumn 2016 and Summer 2017–2018. Cloud properties are derived using data from W-band radars, lidars, and microwave radiometers using an optimal estimation algorithm. The SO clouds tended to have larger liquid water paths (LWP, 115 ± 117 g m^{-2}), smaller effective radii (r_e, 8.7 ± 3 μm), and higher number concentrations (N_d, 90 ± 107 cm^{-3}) than typical values of eastern ocean basin stratocumulus. The clouds demonstrated a tendency for the LWP to increase with N_d presumably due to precipitation suppression up to N_d of approximately 100 cm^{-3} when mean LWP decreased with increasing N_d. Due to higher optical depth, cloud albedos were less susceptible to changes in N_d compared to subtropical stratocumulus. The highest latitude clouds of the datasets, observed along and near the Antarctic coast, presented a distinctly bimodal character. One mode had the properties of marine clouds further north. The other mode occurred in an aerosol environment characterized by high cloud condensation nuclei concentrations and elevated sulfate aerosol without obvious continental aerosol markers. These regions of higher cloud condensation nuclei tended to have higher N_d, smaller r_e and higher LWP suggesting sensitivity of cloud properties to seasonal biogenic aerosol production in the high latitude SO.

1. Introduction

The Southern Ocean's (SO) clouds fields have emerged as one of the lynchpins in our understanding of the Earth's climate system (Frey & Kay, 2017; Gettelman et al., 2020; Kay et al., 2016; Tan et al., 2016). While the region is known for deep midlatitude cyclones, it is the accompanying fields of marine boundary layer (MBL) clouds that seem to be critical to understanding the radiative energy balance of this region (Bodas-Salcedo et al., 2012, 2014, 2016, 2019). Inspired by Trenberth and Fasullo (2010), who showed a high bias in surface-absorbed solar energy by models, studies have increasingly focused on the ubiquity of super-cooled liquid water in SO clouds. Simulations of these clouds too aggressively reduce cloud cover through ice phase precipitation processes (Frey & Kay, 2017; Vergara-Temprado et al., 2018). Recent modeling studies have mitigated this bias through various means and have shown the climate system's sensitivity to these SO MBL clouds (Kay et al., 2016; Tan et al., 2016).

How the properties of liquid phase clouds—especially supercooled liquid phase clouds—vary across the SO remains an important topic. While the meteorology of the SO is predictable, variations in factors that control the local and regional aerosol properties differ considerably from regions north of the Antarctic Circumpolar Current (ACC) to the marginal seas along the Antarctic (Armour et al., 2016; Fossum et al., 2018). While seasonally varying sea surface temperatures and sea ice contribute to the cloud variability (Huang et al., 2016), the Antarctic Circumpolar Current essentially divides the SO into lower latitude temperate and high latitude oceans. Especially in the high latitude SO, seasonal biological productivity results in

Project Administration: Gerald G. Mace, Alain Protat, Ruhi S. Humphries, Melita Keywood, Greg M. McFarquhar
Resources: Gerald G. Mace, Alain Protat, Greg M. McFarquhar
Software: Gerald G. Mace, Ruhi S. Humphries, Ian M. McRobert, Jason Ward, Paul Selleck
Supervision: Gerald G. Mace, Alain Protat, Ruhi S. Humphries, Ian M. McRobert, Melita Keywood
Validation: Gerald G. Mace
Writing – original draft: Gerald G. Mace, Alain Protat, Ruhi S. Humphries, Simon P. Alexander
Writing – review & editing: Gerald G. Mace, Alain Protat, Ruhi S. Humphries, Simon P. Alexander, Ian M. McRobert, Jason Ward, Paul Selleck, Melita Keywood, Greg M. McFarquhar

significant oscillations in sulfate aerosol sources (Ayers & Gras, 1991; Humphries et al., 2016; O'Dowd et al., 1997; Shaw, 1988) that appear to drive variability in cloud properties across the entire oceanic basin between winter and summer (Mace & Avey, 2017; D. T. McCoy et al., 2015; I. L. McCoy et al., 2020). Liquid clouds within this environment respond to large-scale meteorological forcing and moisture transports (Field & Wood, 2007; Govekar et al., 2011; Kelleher & Grise, 2019; Klein et al., 2017; D. T. McCoy et al. 2019; Naud et al., 2018; Wall et al., 2018), as well as the local aerosol environment. The large-scale environment provides the thermodynamic conditions for producing clouds, and the aerosol properties control the detailed processes that determine when and how low-level clouds precipitate (Savic-Jovcic & Stevens, 2008).

In this study, we examine a particular genre of MBL clouds that form a significant component of the total cloud population of the SO. Table 1 summarizes cloud layer occurrence statistics derived from a product that merges geometric layer occurrence data from the CloudSat and CALIPSO satellites (Mace & Zhang, 2014). We find that the SO, defined here broadly as the circumpolar latitude belt from 45°S to 70°S, has an overall cloud fraction of 86%. Of this cloud cover, 63% are single layer clouds. The MBL-based clouds are composed of two classes. Clouds with geometric thicknesses over 1 km tend to be mostly precipitating (as defined by CloudSat radar reflectivity exceeding −20 dBZ). Roughly half of the MBL clouds have geometric thicknesses less than 1 km and exist as nonprecipitating liquid phase layers. Because the nonprecipitating thin clouds have low radar reflectivities or are within 1 km of the surface, they tend to be unobserved by CloudSat (Alexander & Protat, 2018; Marchand et al., 2008). Our focus in this study are these geometrically thin nonprecipitating layers that compose ~1/2 of the MBL clouds in the SO.

In this study, we examine the microphysical properties and latitudinal variability of nonprecipitating Southern Ocean clouds using data collected from Australian Research Vessels between 2016 and 2018. In particular, we investigate dependencies between cloud droplet number (N_d), effective radius (r_e), and liquid water path (LWP) with various factors over the space and time covered by the observations. We consider how these clouds influence the surface solar radiation and the Top of Atmosphere (TOA) albedo, and also how the cloud properties are associated with aerosol regimes characterized during the campaigns.

2. Data and Methods

We use data from recent voyages by Australian vessels between Hobart, Tasmania, and Antarctica (Figure 1). These voyages included a similar set of remote sensing measurements that allow us to apply an identical cloud property retrieval algorithm to each campaign data set. The critical measurements were as follows: (1) radar reflectivity (dBZe) profiles from vertically pointing W-Band radars (hereafter referred to as cloud radars), (2) attenuated backscatter (β_{obs}) profiles from vertically pointing optical lidars, (3) downwelling microwave brightness temperatures T_b at 31 GHz from Radiometric radiometers, and (4) regular radiosonde soundings. We also use surface meteorological measurements, sea surface temperatures, and downwelling solar and infrared broadband fluxes. Aerosol measurements that we use are cloud condensation nuclei (CCN) and sulfate aerosol observations.

Table 1

Vertical Occurrence Data From CloudSat (Stephens et al., 2008) and CALIPSO (Winker et al., 2009) Between 2007 and 2010 Using the Combined Characterization of Mace and Zhang (2014) in the 40°S–70°S Latitude Belt

Total cloud columns meeting MBL, single layer conditions: 17,399,960

Layer Thickness	0–1 km	1–3	3–5
Total	0.47	0.48	0.05
Precipitating	0.08	0.67	0.97

Abbreviation: MBL, marine boundary layer.

Notes. The total row gives the proportion of layers meeting the thickness criteria. Precipitating clouds are defined as those with layer-maximum radar reflectivity from CloudSat exceeding −20 dBZ The number shown is the fraction of the total within that thickness bin. MBL clouds are here loosely defined as those with bases below 2 km.

The first of these voyages was aboard the Australian Research Vessel (RV) Investigator in March and April of 2016 (Mace & Protat, 2018a, 2018b, hereafter MP18a and MP18b, respectively). Unlike the other voyages, the 2016 voyage, hereafter referred to as Clouds Aerosols Precipitation Radiation and atmospheric Composition Over the SoutheRN ocean (CAPRICORN) I spent its nearly 5-week duration north of 53°S. Much of CAPRICORN I was spent in the vicinity of 45°S and 142°E servicing Southern Ocean Time Series buoys (Schulz et al., 2012). In total, we use 137 h of nonprecipitating liquid cloud data from CAPRICORN I.

CAPRICORN II was an observational campaign on board the Australian RV Investigator during a voyage from Hobart to the Antarctic Shelf between 11 January and February 21, 2018. CAPRICORN II occurred in conjunction with the U.S. National Science Foundation-sponsored Southern Ocean Cloud Radiation Aerosol Transport Experimental Study
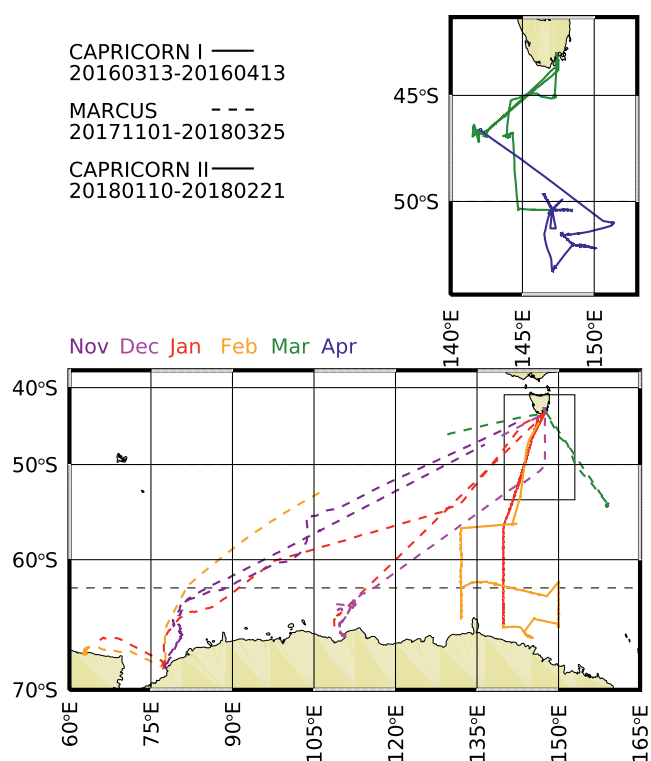
Figure 1. Voyage tracks taken by the R/V Investigator and Aurora Australis during CAPRICORN I and II and MARCUS. 50°S and 62.5°S (marked by a dahsed line) denote the boundaries between the northern, middle, and southern analysis domains. CAPRICORN, Clouds Aerosols Precipitation Radiation and atmospheric Composition Over the SoutheRN ocean; MARCUS, Measurements of Aerosols, Radiation and Clouds over the Southern Ocean.
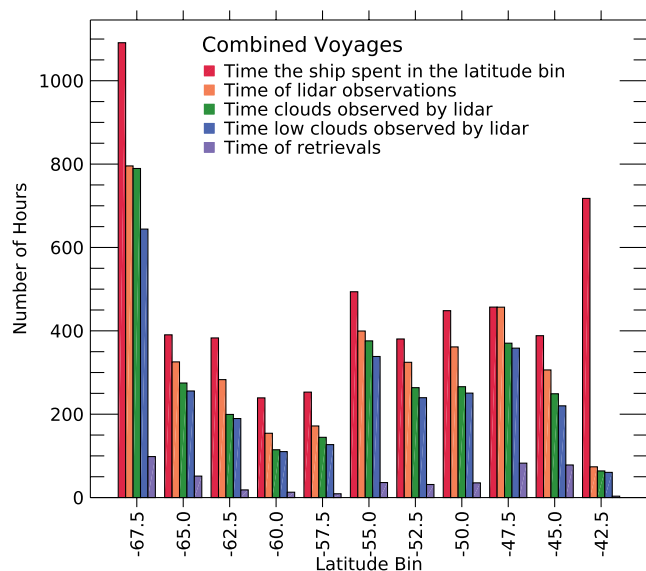

Figure 2. Latitudinal distributions of time spent and observations obtained from the three voyages used in this study. The legend explains the meaning of the various histograms.

(SOCRATES) campaign (McFarquhar et al., 2020). SOCRATES featured 15 flights by the National Center for Atmospheric Research (NCAR) Gulfstream V. CAPRICORN II included the same cloud instruments that participated in CAPRICORN I as described in MP18a. This study focuses on data from a Doppler Cloud radar, a 355 nm Lidar, and a two-channel microwave radiometer. During the 7-week voyage, approximately 300 radiosondes were launched on a 3–6 hourly schedule depending upon the weather.

The CAPRICORN II voyage track was mostly determined by oceanographic objectives that included 88 preplanned stations where water column soundings were made. Stations were occupied between the 130°–150°E meridians during the voyage with a delay at each station for 6–24 h. Stations were separated by approximately 50 km. Small steps with roughly half-day delays allowed for a unique characterization of the aerosol, cloud, and thermodynamic properties. RV Investigator passed south of 50°S on 18 January and 60°S on 27 January, both along the 140°E meridian and reached the southernmost point of the voyage on 2 February near the seasonal ice edge at 66°S. Investigator then remained south of 60°S occupying stations between 132°E and 150°E until 15 February. Following the final oceanographic station occupied near 57°S and 132°E on 16 February, Investigator made a brief eastward excursion to coordinate with a GV flight on 18 February near 57°S, 140°E and another minor diversion to coordinate with a descending overpass of the CALIPSO satellite at 48°S and 144°E on 20 February. We use 78 h of nonprecipitating MBL clouds from CAPRICORN II.

The MARCUS campaign featured components of the U.S. Department of Energy's (DOE) Atmospheric Radiation Measurement (ARM) program's second Mobile Facility (AMF2) deployed onboard the Australian ice breaker RSV Aurora Australis during the 2017–2018 Antarctic summer season as it made resupply voyages to the East Antarctic. Four voyages took place from early November 2017 through March 2018 (Figure 1) and all departed from and arrive back to Hobart. The instrumentation that we use are as follows: (1) β_{obs} from a Micropulse Lidar, (2) T_b from a Radiometrics microwave radiometer (Liljegren et al., 2001), and (3) radar reflectivity profiles from the Marine W-Band ARM Cloud Radar (M-WACR). Radiosondes were launched on a 6-hourly schedule when away from Hobart. Because of the resupply objectives, the ship steamed from Hobart to and from the Antarctic coast directly, while avoiding bad weather and as much of the early season thick sea ice as possible. Each 1-way transit to and from Antarctica took from 7 to 10 days, depending on destination. The ship's speed was reduced in sea ice, and the ship spent up to 2 weeks at each station for the resupply operations. The final voyage of the season to and from Macquarie Island (55°S) occurred during the first 2 weeks of March. In total, we use 265 h of nonprecipitating cloud data from Marcus.

Figure 2 provides a graphical view of the combined data. The overall larger amount of time in the latitudes north of and including 55°S are due to the ship tracks of the three campaigns. MARCUS spent several weeks in total at the Antarctic Stations, which explains the large number of hours at the southernmost latitudes. The most northern bin denotes time spent in Hobart during MARCUS when the instruments were not operated. The high value of cloud fraction near 85% is evident, with more

than half of these observations being from clouds with bases below 2 km. The similarities of these statistics with those in Table 1 are evident. The retrievals that are described in the next section are implemented much less often due mostly to limitations that require the clouds to be nonprecipitating and a requirement for the microwave radiometer window to be dry. With sea spray and liquid precipitation, this limited the applicability of the algorithm.

3. Method

We seek to examine the properties of a dominant genre of clouds that influences the radiative properties and cloud optical depth feedbacks in the Southern Ocean. Nonprecipitating liquid clouds are ubiquitous across the Southern Ocean and compose roughly half of all clouds in the MBL (Table 1). From an analysis standpoint, the single-phase liquid and nonprecipitating clouds require a minimum of assumptions in developing algorithms needed to infer their properties, thereby minimizing uncertainty. In this study, we implement an optimal estimation (OE) algorithm that derives the layer mean LWP, the layer mean effective radius (r_e), and the cloud droplet number concentration (N_d.) Reasoning that β_{obs} constrains approximately the second moment of the droplet size distribution (DSD), dBZe constrains the sixth moment of the DSD in the Rayleigh scattering regime, and T_b provides a vertically integrated constraint on the condensed water (LWP), the measurement combination uniquely constrains the DSD. The cloud radars were on stabilized platforms for CAPRICORN II and MARCUS but not for CAPRICORN I. We base our retrieval methodology on the approach described in Mace and Protat (2018b). However, we describe the algorithm in detail because of several improvements made since that initial study. Our basic assumptions, however, are mostly unchanged.

To illustrate our methodology, we use a time section of measurements from CAPRICORN II collected on January 29 when the ship was in the vicinity of 64°S and 140°E (Figure 3). This day featured an overcast MBL cloud layer that precipitated until late in the UTC day. There were eight soundings launched during these 24 h.

3.1. Initial Data Processing and Calibration

The lidar measurements that we use were collected from a 532 nm Micropulse Lidar for MARCUS and from a 355 nm RMAN lidar system in CAPRICORN I and II (See Royer et al. 2014 and MP18a for a brief description of the RMAN system). Both systems provide an elastic backscatter and depolarization channel. While the RMAN system provides a Raman scattering channel, the system's sensitivity is such that long integration times in cloud-free tropospheric air are required for calibration (Alexander & Protat, 2019). In our earlier work (MP18b), we relaxed the β_{obs} profile to theoretical Rayleigh β_{obs} profiles from clear sky nights. However, the calibration of the lidar drifts significantly on timescales of hours, resulting in large uncertainties in β_{obs} that we accounted for in our earlier work by increasing the error in β_{obs} in the OE algorithm. Here, we implement a calibration method that is particularly suitable for the clouds that we are considering using a methodology described first by O'Connor et al. (2004). From the early work of Platt et al. (1999) and following Li et al. (2011), we express the observed attenuated backscatter as

$$\beta_{obs}(z) = \beta(z)e^{-2\int\sigma dz}. \tag{1}$$

β_{obs} is the result of two-way attenuation through the cloud to a point z in the layer and σ is the extinction coefficient with units of inverse length where σ is expressed in terms of the lidar ratio, $S = \dfrac{\sigma}{\beta}$. A factor η accounts for the addition of photons to the observed signal due to multiple scattering in optically dense clouds. We can then write (1)

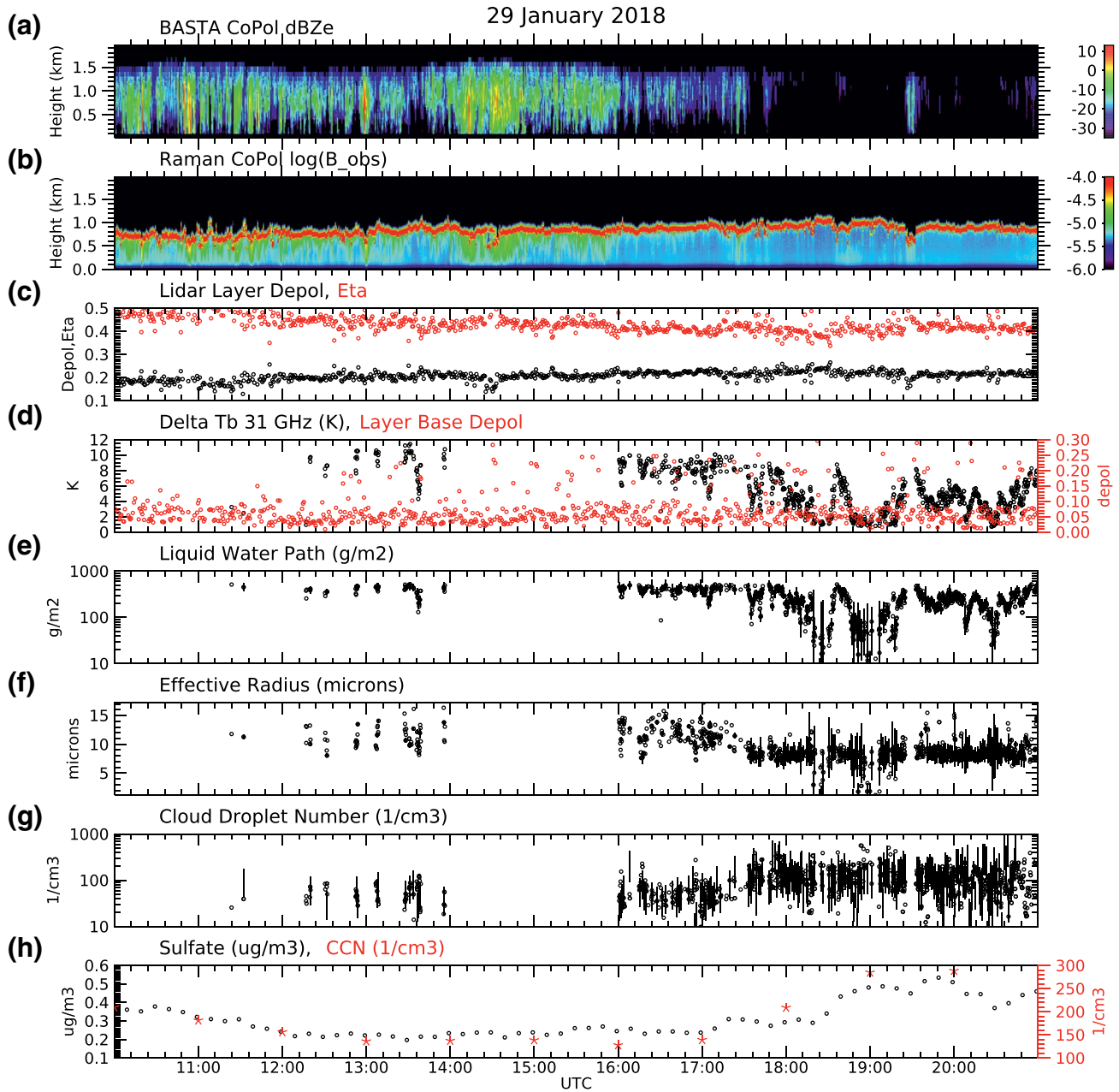$$\beta_{obs}(z) = \beta(z)e^{-2\eta Sr} \tag{2}$$

Figure 3. January 29 Case Study collected during CAPRICORN II. (a) radar reflectivity from the BASTA Cloud Radar. (b) Lidar attenuated backscatter, (c) lidar layer-integrated depolarization ratio (red) and multiple scattering factor (black), (d) difference of 31 GHz Tb from cloud-free sky (black) and lidar depolarization ratio at cloud base. (e) Retrieved Liquid water path with uncertainty marked by the error bars. (f) retrieved effective radius with error bars. (g) retrieved cloud droplet number with error bars. (h) Aerosol Sulfate mass and CCN at 0.5% supersaturation. CAPRICORN, Clouds Aerosols Precipitation Radiation and atmospheric Composition Over the SoutheRN ocean; CCN, cloud condensation nuclei; MARCUS, Measurements of Aerosols, Radiation and Clouds over the Southern Ocean.

where we are averaging over the layer through a range r. Defining the layer-integrated total attenuated backs-

catter as $\gamma = \int \beta_{\parallel+\perp}$ and the layer integrated depolarization ratio as $\delta = \frac{\int \beta_{\perp}}{\int \beta_{\parallel+\perp}}$ we express $\eta = \left(\frac{1-\delta}{1+\delta}\right)^2$ (Hu

et al., 2009). Platt et al. (1999) relates S with η according to $S\eta = \dfrac{1-T^2}{2\gamma}$ and where T is the layer transmittance. When the layer is fully attenuating (T = 0) and

$$S = \frac{1}{2\eta\gamma} \tag{3}$$

O'Connor et al. (2004) and Hu et al. (2009) show that S varies over a narrow range in liquid water clouds with an average near 18.8. We confirmed this by examining S calculated from Mie theory using observed DSDs collected in water clouds during Rain in Clouds over the Ocean (RICO; Rauber et al., 2006). We found that S and r_e vary systematically (Mace et al. 2020), with a small dynamic range of S from 17 to 19 for >90% of all cloud DSDs observed during RICO. This range is small relative to the calibration uncertainty in measured β_{obs} for elastic lidars and the assumptions used to derive Equation 3. Following O'Connor et al. (2004), therefore, we fix S in water clouds at a mean value of 18.7 (the mean value we found from the RICO DSDs) that corresponds to an assumed r_e of ~10 μm. We effectively calibrate the lidar signal by adjusting γ by a factor that gives $S = 18.7$ on a profile-by-profile basis. This auto-calibration (O'Connor et al.'s term) method allows us to have a physically consistent characterization of β_{obs} independent of using the Rayleigh method in nighttime cloud-free skies. We show the results of this method applied to the 29 January data in Figure 3. A factor with an average of ~3.5 is applied to the observed lidar β_{obs} on this day to achieve an S of 18.7. This method's limitations are apparent since we implicitly assume that the layer-mean effective radius is approximately 10 μm. However, as we show below, the OE inversion methodology allows the final solutions to depart from this assumption.

As the lidar signal penetrates into an optically thick cloud β_{obs} becomes dominated by multiple-scattered light and becomes increasingly depolarized relative to the transmitted signal. This effect is quantified by η. The 355 nm system will have a sharper forward diffraction peak than the 532 nm MPL system, resulting in less integrated backscatter and lower values of η. This weaker signal is compensated by the lower background signal in the UV channel compared to the MPL. Typically, β_{obs} increase from cloud base to a maximum value a few range bins into the layer, and β_{obs} then begin exponential decay as the signal becomes increasingly dominated by multiply scattered light. Following Li et al. (2011), If we take the natural logarithm of both sides of Equation 1, we can write $\eta\sigma = -\dfrac{\ln\beta_{\text{obs}} - \ln\beta}{2r}$ where the right-hand side is the logarithmic decay of the multiply scattered signal with depth. Because we have estimated η from measurements (independent of calibration), we can estimate σ in the optically thick part of the layer beyond the peak in β_{obs} using linear regression. Li et al. (2011) compare σ derived from this method to estimates of σ derived from passive reflectances and find an uncertainty of ~13%. This method's accuracy depends on calculating the rate at which the signal decays with depth in the layer. In practice, we fit a regression line to β_{obs} at heights above the layer maximum in β_{obs} until the signal is a factor of 2 above the lidar noise floor. We determine the lidar noise level from the mean β_{obs} well above the fully attenuating cloud layer. The goodness of the linear regression fit depends on the number of measurements in this range. The accuracy depends on the vertical resolution of the lidar measurements when σ is large. The vertical resolution of the RMAN and MPL data during these campaigns is 15 m. We find that for clouds with σ less than 50 km^{-1}, we can use 3–5 data points to estimate the slope. When σ becomes larger than ~75 km^{-1}, we find that typically only 2–3 points are available, and the uncertainty in σ becomes large. We found this to be a limiting concern in only a few cases near the coast of Tasmania when the clouds existed within continental air masses. Figure 3 shows lidar data from a case collected on 29 January. We find that the layer observed on 29 January had a mean σ of ~20 km^{-1} varying from 10 to 40 km^{-1}. We discuss this case in more detail below.

To separate liquid phase clouds from clouds that are mixed phase, we follow the approach used in MP18A, where we examine the sub cloud for measurable signal depolarization when the cloud radars observe precipitation. In warm clouds, we found that the vertically resolved sub cloud depolarization ratios were reliably less than 0.1. In situations when the precipitation was known to be frozen, the sub cloud depolarization ratios typically exceeded 0.2. Figure 3d shows a time series of sub cloud depolarization ratios from a cloud layer with a base temperature near −8°C that was producing occasional frozen precipitation at
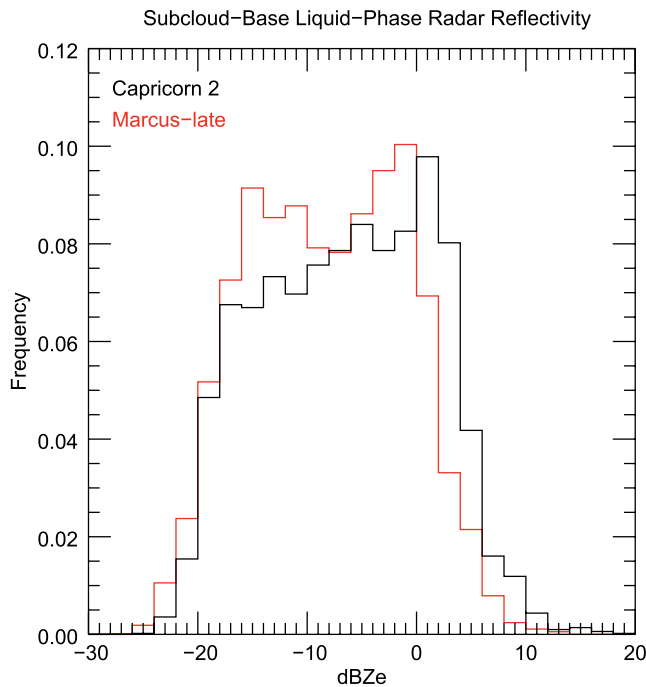
Figure 4. Comparison of sub cloud radar reflectivity from liquid hydrometeors observed by the calibrated BASTA Cloud radar and the MARCUS MWACR during the months of January and February (red). MARCUS, Measurements of Aerosols, Radiation and Clouds over the Southern Ocean.

the surface noted by observers. We see pockets of ice phase precipitation from this layer, but most of the precipitation was liquid and did not reach the surface.

A known issue exists with the MARCUS MPL during the first half of the campaign (through Voyage 2 that ended on 12 January) where the window through which the MPL viewed the atmosphere changed the polarization state of the laser light resulting in a minimum depolarization ratio measured by the instrument to be ∼0.2. This issue was corrected in Hobart on January 15, 2018, before Voyage 3. Since we found that when ice was present near the cloud base, the depolarization ratios typically exceeded 0.4, we use a threshold of 0.3 for the early MARCUS voyages to identify the presence of ice. We use a sub cloud depolarization ratio of 0.2 as a threshold for later MARCUS and CAPRICORN I and II.

The vertically pointing millimeter radars used in CAPRICORN I and II and MARCUS were W-Band Doppler systems. In CAPRICORN I and II, the radars used were the Bistatic Radar System for Atmospheric Studies (BASTA; Delanoë et al., 2016). We calibrated the BASTA radar observations using statistical comparisons between BASTA, the K-band micro rain radar, and K-band and W-band T-matrix calculations using the ODM470 disdrometer observations from the mast (see Klepp et al., 2018 for more details and CAPRICORN I results). We also compared BASTA cloud radar observations with CloudSat reflectivities using the technique outlined in Protat et al. (2011) from deployments surrounding the CAPRICORN experiments. These comparisons allowed us to confirm the calibration figures derived from the disdrometer and micro rain radar comparisons (not shown).

As noted recently by Kollias et al., (2019), the ARM millimeter radars are subject to significant calibration uncertainties. Specifically, Kollias et al, (2019) compared the M-WACR measurements with CloudSat. They noted that the M-WACR calibration ranges from 4 to 8 dB lower than the well-calibrated cloud radar on CloudSat (Tanelli et al., 2008). Such a calibration uncertainty is prohibitive for quantitative use of the radar reflectivities, and no direct means of calibrating the M-WACR system were available during MARCUS. Furthermore, during late 2017 and early 2018, CloudSat was involved in a transition in orbit, so regular data were not collected. To establish some means of assessing the calibration of the M-WACR, we reason that the RSV Aurora Australis and the RV Investigator were collecting data in a similar region during a common period and aspects of their data should, therefore, be similar. We expect that the radar reflectivity statistics of subcloud liquid precipitation should be similar because of their common frequency. Therefore, we examine the radar reflectivity statistics in the 200 m above the radars and up to 1 range bin below the lidar cloud base during light liquid precipitation (Figure 4). We find that the M-WACR is offset low from the calibrated BASTA radar results during CAPRICORN II. Adding 4.5 dB to the M-WACR subcloud precipitation results causes the two histograms to come into alignment (Figure 4 shows the uncorrected MARCUS results). This offset is consistent with the findings of Kollias et al. (2019), and therefore, in all results presented henceforth, this offset has been added to the M-WACR dBZe measurements.

3.2. Algorithm to Derive N_d, LWP, and r_e

The nonprecipitating liquid phase clouds that we examine are assumed to be composed of a single mode of droplets that can be described by a modified gamma distribution,

$$N(D) = N_0 \left(\frac{D}{D_0}\right)^\alpha \exp\left(-\frac{D}{D_0}\right) \tag{4}$$

where $N(D)$ is the droplet number per unit size and has units of cm^{-4}. N_0, D_0, and α are characteristic number, diameter and the shape parameter of the DSD. All units are cgs unless specified otherwise. This simple

integrable function allows us to express the microphysical quantities, N_d (cloud droplet number), q (liquid water content), and r_e (effective radius) with the following expressions,

$$N_d = N_0 D_0 \Gamma(\alpha + 1)$$

$$q = \rho \frac{\pi}{6} N_0 D_0^4 \, \Gamma(\alpha + 4) \tag{5}$$

$$r_e = \frac{D_0}{2}(\alpha + 3)$$

where we use the recursion properties of the gamma function in the ratio of the third and second moments of $N(D)$ for r_e. See Posselt and Mace (2014, their Appendix B). Similarly, we can relate observable quantities to $N(D)$ using the appropriate moments. The radar reflectivity parameter, Z_e, can be written as the sixth moment of $N(D)$

$$Z_e = 10^{12} N_0 D_0^7 \Gamma(\alpha + 7) = 10^{12} \frac{48}{\pi} r_e^3 q F_6. \tag{6}$$

where the constant 10^{12} converts from cgs to the typical units for Z_e of $\mathrm{mm^6 \, m^{-3}}$ and $F_6 = \dfrac{(\alpha + 6)(\alpha + 5)(\alpha + 4)}{(\alpha + 3)^3}$

arises from the recursion properties of the gamma function. Equation 6 assumes that the droplets remain small with respect to the wavelength of the radars (~3 mm) so that the Rayleigh approximation is valid. The lidar backscatter and extinction coefficients are similarly derived from second moments of N(D) times $\frac{\pi}{4}$ multiplied by the extinction efficiency (here assumed to be 2) and the backscatter efficiency which is assumed constant at 0.12 (MP18b), respectively (see Posselt & Mace, 2014).

The OE inversion methodology is convenient for arriving at solutions to problems using disparate data streams that account for uncertainties in observations and assumptions given prior statistics (Maahn et al., 2020; Mace et al., 2016). The method we use is adapted from Rodgers et al (2000) and minimizes a cost function using Gaussian statistics and Newtonian iteration. In a problem with several degrees of freedom and inherent uncertainties in observations and forward models, it is often necessary to begin the iteration with a physically reasonable first guess to avoid converging on an unphysical local minimum of the cost function generated by uncertainties. To arrive at this first guess, we combine Z_e, σ derived from β_{obs} and T_b. We use a simplified analytical model relating T_b and LWP (MP18b),

$$\delta T_b = T_{eff} \left(1 - \exp\left(-\frac{3}{2} a_b \mathrm{LWP} \right) \right) \tag{7}$$

where δT_b is the increase in 31 GHz T_b caused by the presence of the cloud layer and $a_b = 1.712$ is the approximate mass absorption coefficient in cgs units (MP18b) derived from Mie theory. The measurements then constrain the mass and the cross-sectional area of what we assume to be a layer-mean DSD. We then iterate to estimate α using Z_e as a constraint. Reasonably often, however, the cloud radars do not detect the nonprecipitating cloud layers. This occurs approximately 25% of the time for CAPRICORN I and II and 15% of the time during MARCUS (we estimate the M-WACR was ~5 dB more sensitive than the BASTA radars). In such cases we fix our initial estimate of α at a mean value of 2.5 derived from in situ data collected during SOCRATES. This first guess N(D) is then used to begin the OE iteration.

The OE algorithm that we employ is identical to that described in MP18b starting at Equation 12 of that study, with all observations interpolated to the BASTA radar's time indexes. The main difference between the earlier work and here is that we calibrate the β_{obs} measurements using the O'Connor et al. (2004) method. We constrain the first guess by the extinction coefficient derived from the lidar data. Because we start with a microphysical estimate that already reasonably replicates the measurements, the final solution does not

depart substantially from the first guess. Therefore, the constraints provided by the lidar-derived extinction are a new feature of this updated approach. Another essential difference between MP18b and this analysis is that we use prior statistics derived from the in-situ data collected during SOCRATES (Wang et al., 2020). Therefore, the algorithm produces results that are statistically similar to this specific prior knowledge of SO clouds. We also focus on N_d in this study. While we do not retrieve N_d specifically, we derive it from the retrieved LWP, r_e, and α. We use the uncertainties of the retrieved quantities with a bootstrap approach (Kirk & Stumpf, 2009) to estimate the uncertainty in N_d. We discuss uncertainty in more detail below, where we explain and also discuss validation of the algorithm using solar flux radiative closure.

4. Results

4.1. January 29 CAPRICORN II Case Study

During the latter half of the UTC day on January 29, 2018, the RV Investigator was stationary near 63.5°S and 139.8°E in the cold sector of a deep cyclone that had passed early during the UTC day on 28 January. On 29 January, the low-pressure system was centered near 65°S and 170°E. At the RV Investigator location, surface temperatures were just below freezing during much of the day on 29 January. Occasional light snow was reported from an overcast stratocumulus layer by radiosonde operators during 3-hourly launches. Winds were sustained southerly around 20 knots, and surface pressures rose steadily from a minimum of 965 hPa early on 28 January to 985 hPa at 18 UTC to 990 hPa by 00 UTC on 30 January. Figures 3a and 3b show that at 15 UTC on 29 January, the cloud layer base was near 750 m and the radar layer tops extended to ~1.5 km. The BASTA cloud radar observed occasional light precipitation from this overcast layer. Lidar depolarization ratios suggest that the sub cloud precipitation was mostly liquid with brief periods of ice phase precipitation. The ice phase precipitation was typically associated with peaks in radar reflectivity. The MRR recorded light precipitation during several brief periods (less than a few minutes in duration) before 12 UTC on 29 January. However, no precipitation was observed by MRR after 12 UTC, and no precipitation was recorded by the ship rain gauge during the entire day suggesting that the precipitation was very light. The sounding at 1600 UTC (not shown) indicates that the lifting condensation level (LCL) was near the cloud base at −8°C with a marine inversion base near 1.3 km at −14°C. The inversion top was near 1.45 km. The 1600 UTC sounding indicates that the MBL was well mixed from the surface to the cloud base. After 1600 UTC, the light precipitation observed by the cloud radar became less frequent. After 18 UTC, the radar reflectivity of the layer fell below the detection threshold of the cloud radar. The microwave radiometer and lidar shows that the cloud layer was persistent through 21 UTC. Lidar-derived extinctions in this layer were steady between 30 and 40 km⁻¹. The RMAN lidar well characterized this layer with uncertainties in the extinction in the range of 20%–30%.

As the precipitation mostly ceased after 16 UTC, we can derive cloud properties from the remote sensing data in the supercooled liquid cloud layer using the method described above. In the hour between 16 and 17 UTC, water paths were steady between 200 and 300 g m⁻² (Figure 3e) with uncertainties near 15%, effective radii were variable. However, they averaged 12 μm (Figure 3f) with uncertainties in the 10% range. N_d was mostly below 50 cm⁻³ (Figure 3g) with uncertainties of approximately 70%–80%. As the precipitation ceased and the radar reflectivity decreased to below the detection threshold of the BASTA cloud radar, the water path of the layer gradually decreased and became variable (Figure 3e). Note that as the reflectivity dropped below the BASTA detection threshold, the uncertainty of r_e and N_d increases. This increase in uncertainty is the result of how we handle the OE inversion when the radar is unable to sense the layer. Because we know the radar detection threshold, we know that the maximum radar reflectivity in the layer must be lower than that threshold. Therefore, we set the radar reflectivity to −35 dBZe and we assume that the uncertainty in that reflectivity is 5 dB. This assumption allows us to use the measurements of LWP and σ and use the knowledge that the dBZe is lower than the detection threshold. The uncertainties in r_e, then increase to be on the order of 50%, and the uncertainties in N_d to ~120%.

A notable aspect of this case study is that before the layer became undetectable by the cloud radar, r_e and N_d begin opposite trends with N_d increasing and r_e decreasing. This change begins near 17:10 UTC, and by 17:30 UTC, r_e is steady near 8 μm while N_d effectively doubles to be in the 100 cm⁻³ range. These changes then persist through the remainder of the period, even when the layer is observable by radar at a few instances. We note this because we see an associated change in aerosol properties and chemical composition

recorded at the surface about an hour after the change in the cloud layer (Figure 3h). CCN at 0.55% supersaturation increases from ~150 to 300 cm^{-3}, and the sulfate mass concentration in submicron aerosol increases from 0.2 to 0.5 μg m^{-3} as measured by the Time of Flight Aerosol Chemical Speciation Monitor (Tof-ACSM; Fröhlich et al., 2013). The step increases in aerosol properties are consistent with increased N_d and decreased r_e. We note that LWP becomes variable and decreases but does not seem to be responding in a similar stepwise fashion as do r_e and N_d. The lidar data and associated derived products do not demonstrate an abrupt transition at this time. We note that over the period shown in Figure 3, the cloud base as derived from lidar β_{obs} lifted gradually and evidence for sub cloud precipitation became more sparse. A careful examination of the δ and η also demonstrates a gradual increase and decrease, respectively, between 11 and 20 UTC. These changes would be consistent with droplets becoming smaller with time and N_d increasing although σ remains near 20 km^{-1} through the period.

The ~1 h time offset in changes between the surface aerosol and cloud layer is curious. Recall that the 16 UTC sounding showed the MBL to be well mixed. However, a sounding launched at 19 UTC showed that the inversion base had descended to 1.2 km (top remained near 1.4 km), and the surface layer was decoupled from the deeper MBL by a weak inversion at 200 m. Below 200 m height, the humidity was largely unchanged, while above 200 m, the profile had dried considerably in the intervening 3 h. It is plausible that free tropospheric air containing biogenic sulfate aerosol had mixed into the MBL, reducing humidity and influencing cloud properties. Because the MBL was decoupled, it took some time for that change to be mixed to the surface.

We further note that this step-change in aerosol chemistry and CCN is similar to events described by Humphries et al. (2016) at similar latitudes (see also Alroe et al., 2020). Up to this time during CAPRICORN II, sulfate concentrations had remained mostly below 0.2 μg m^{-3}, and the step change on 29 January to values above 0.4 μg m^{-3} marked the beginning of elevated surface CCN and sulfate that persisted until 4 February while the ship operated south of 65°S. Markers of continental air mass origin such as radon were absent during this period. N_d remained mostly larger than ~100 cm^{-3} until 4 February. Between 5 February and 15 February, poor weather precluded cloud retrievals. See McFarquhar et al. (2020) their Figure 19 for a daily summary of CAPRICORN II cloud and aerosol time series that illustrate these events.

4.2. Cloud Properties and Radiative Effects

One of the key motivating factors for the SO measurement campaigns is the surface solar radiation bias common to many climate models. However, actual measurements of surface solar radiation and associated clouds are rare in the SO. Here, we explore the properties of a genre of clouds that are key components of this region's surface energy balance. We combine data from the MARCUS and CAPRICORN campaigns into a single data set that brackets the austral summer months from November through mid-April. The latitude range extends from the East Antarctic coast, where the Aurora Australis spent several weeks of the summer campaign to Hobart's latitude near 42°S, which is the common home port for both vessels. In total, we consider 480 h of retrieved cloud properties. We find that the nonprecipitating clouds have a mean LWP of 90 g m^{-2} with a standard deviation of about 100 g m^{-2}, r_e near 8.7 ± 3 μm, and N_d near 90 cm^{-3} with about a 200% standard deviation (Figure 5). In Figures 5b and 5c, we compare the retrieved values with distributions derived from the SOCRATES in situ microphysical measurements where we exclude the precipitation mode in bimodal liquid droplet distributions (Mace et al., 2016). We have also compared liquid water content (q) by dividing the retrieved LWP by the layer thickness with the q measured in situ and found similarly unbiased agreement (not shown). We expect the offset that we see in the in situ and retrieved N_d distributions. The larger N_d values in the retrieved cloud properties are derived from data near Antarctica and also close to Tasmania. The SOCRATES data set does not include samples at those latitudes (see McFarquhar et al., 2020 and below). We note that the retrieved cloud properties are in broad agreement with similar quantities derived from A-Train data (Mace & Avey, 2017; D. T. McCoy et al., 2015). A-Train data show that these clouds' microphysical properties vary seasonally with higher N_d and lower r_e during summer associated with changes in aerosol derived from biogenic sources. Because the A-Train is limited to layers above 1 km in altitude, we generally find lower water paths than in Mace and Avey (2017).

In Figure 5, we also show the uncertainty statistics in the retrieved microphysical quantities. Consistent with our discussion of the case study in Figure 3, we find that LWP and r_e are retrieved typically to within a
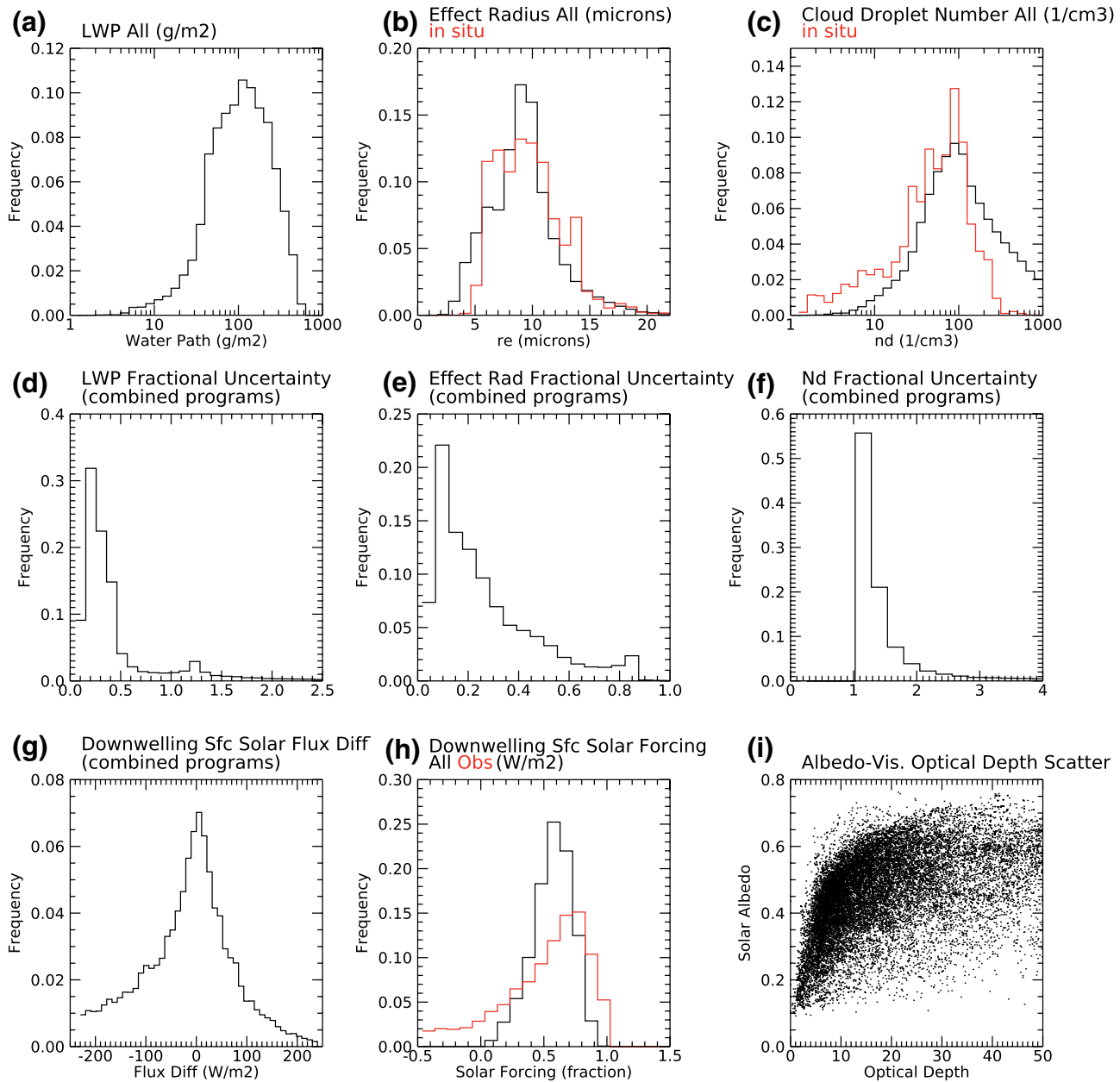
Figure 5. Cloud and radiation property frequency distributions compiled from the retrieved microphysical properties using data from MARCUS and CAPRICORN I and II. Red histograms show observations compiled from in situ airborne data from SOCRATES (b) and (c) and from the ship pyranometer (h). (a) Liquid water path, (b) Effective radius with red showing the effective radius frequency from the SOCRATES in situ data (c) Cloud Droplet Number Concentration with red as in (b) (d) uncertainty distribution of LWP, (e) uncertainty distribution of effective radius, (f) uncertainty distribution of cloud droplet number. (g) Distribution of the difference of calculated downwelling solar flux from that observed at the ship. (h) Calculated fraction of the downwelling solar flux at the surface removed from the clear sky flux by the clouds. (i) scatterplot of albedo calculated from the cloud properties as a function of visible optical depth. CAPRICORN, Clouds Aerosols Precipitation Radiation and atmospheric Composition Over the SoutheRN ocean; LWP, liquid water paths; MARCUS, Measurements of Aerosols, Radiation and Clouds over the Southern Ocean.

few tens of percent. However, N_d is not known to within a factor of 2 generally. We expect high uncertainty in N_d. Because N_d is the DSD's zeroth moment, the remote sensing measurements do not directly constrain N_d. β_{obs} being a function of the second moment of the DSD comes closest. However, even β_{obs} is still two orders removed, meaning that the DSD's droplet sizes that control N_d are typically not those that control the cross-sectional area and β_{obs}. Constraining the cross-sectional area does not constrain N_d without additional assumptions regarding correlations among the DSD moments or the functional form of the DSDs. We,

therefore, rely on correlations among the microphysical quantities in our prior data. The natural variability in the covariances that exist in the prior data combined with uncertainties in the retrieved quantities drives the resulting uncertainty in N_d shown in Figure 5.

We use solar radiation measured at the surface as a means of vicarious validation of the retrieved microphysics. We assume that retrieval biases would show up as overall biases in the solar flux comparison. Following the method described in Berry et al. (2019, 2020), we calculate the downwelling solar flux at the surface using the two-stream radiative transfer model described by Toon et al. (1989) as modified by Kato et al. (2001). For solar zenith angles less than 80° with no higher cloud layers, we compare the downwelling solar fluxes measured on the ships with those calculated using the retrieved microphysical quantities. There are challenges with such an approach since we only measure the cloud properties at the zenith, while surface radiation measurements are hemispheric. We then assume that those properties are spread over a plane parallel sky. Using this method, we found extended periods when the flux was biased high or low over periods of hours. Such biases caused us to remove 3 days of data from the CAPRICORN I data, 6 days from the CAPRICORN II data, and 4 from MARCUS. In most of these poorly rendered cases, it seems that the MWR or radar radome or both were wet from precipitation or sea spray, or the lidar window was covered by condensed sea salt – operating sensitive instrumentation at sea in the Southern Ocean is challenging. We conducted this manual filtering on daily timescales. If a day appeared on average reasonably unbiased, we kept that day in the data set.

What we find after removing bad days is that the flux difference (calculated flux minus observed flux) has a modal value of $-4\ \mathrm{W\,m^{-2}}$ with a mean, median, and standard deviation of 25, 18, and $63\ \mathrm{W\,m^{-2}}$, respectively (Figure 5g). Because the low-level clouds are typically cellular even when overcast, they allow for variable transmission of sunlight and three-dimensional radiative effects. It is not unexpected that the bias is negative at higher values of flux. Direct beam sunlight reaching the pyranometers at higher zenith angles or reflection from cloud sides would cause such a bias. Note also the negative solar forcing in the red histogram derived from the observed fluxes in Figure 5h as evidence of these 3d effects. While our goal is to show an unbiased comparison, the distribution in Figure 5g has a -6% bias suggesting that the retrieved microphysical properties are physically reasonable but with possible low (high) biases in LWP (r_e) or offsetting biases in both that are unknown. Unfortunately, no airborne validation is available. While the NCAR GV aircraft flew over the R/V Investigator several times during CAPRICORN II, these instances occurred when the MWR was wet due to drizzle or sea spray, and we could not conduct retrievals.

As discussed in Protat et al. (2017), MBL clouds like those considered here have a significant impact on the downwelling solar flux at the surface (Figure 5h) and TOA (Figure 5i). Expressing the net solar cloud radiative effect (CRE) as one minus the fraction of the downwelling cloudy flux divided by the clear sky solar flux, we find a mean value of 0.52 with a standard deviation of 0.33. The effect of these clouds then is to remove typically between 1/3 and 2/3 of the solar radiation from the net surface fluxes when they are present. The solar forcing derived from the actual flux observations (normalized by the calculated clear sky) shows a broader distribution that extends to negative values. This type of bias would indicate reflection from cloud sides or reflection from and blocking sunlight by the ships' superstructures.

The albedo (A) of these clouds are, on average, 0.47, with a standard deviation of 0.12. A question we address below in more detail is how the radiative effects of these clouds are susceptible to changes in microphysics. The scatter plot of A versus optical depth shows that most of these clouds exist at optical depths that are lower than ∼20. Painemal and Minnins (2012) examine data from eastern ocean basin stratocumulus and find significantly lower A (0.2–0.3) from lower LWP (∼60 g m^{-2}) and higher N_d (150–200 cm^{-3}) clouds. The analysis of Abel et al. (2010) of the SE Pacific stratocumulus data shows that N_d tended to decrease away from the coastal regions to values near 100 cm^{-3}. Water paths also increased to values over 150 g m^{-2}. Lu et al. (2009), analyzing airborne stratocumulus data offshore of California, showed a similar tendency with lower N_d and larger r_e with distance from continental influences.

We can better understand the Southern Ocean clouds, the processes involved in their maintenance, and their effects on the energy balance by examining relationships among the variables. In particular, we examine how the microphysics and radiative effects are interrelated. This thinking has heritage back to at least Twomey (1977), who showed dependencies of A on N_d, that is, the Twomey Effect. Because A is a
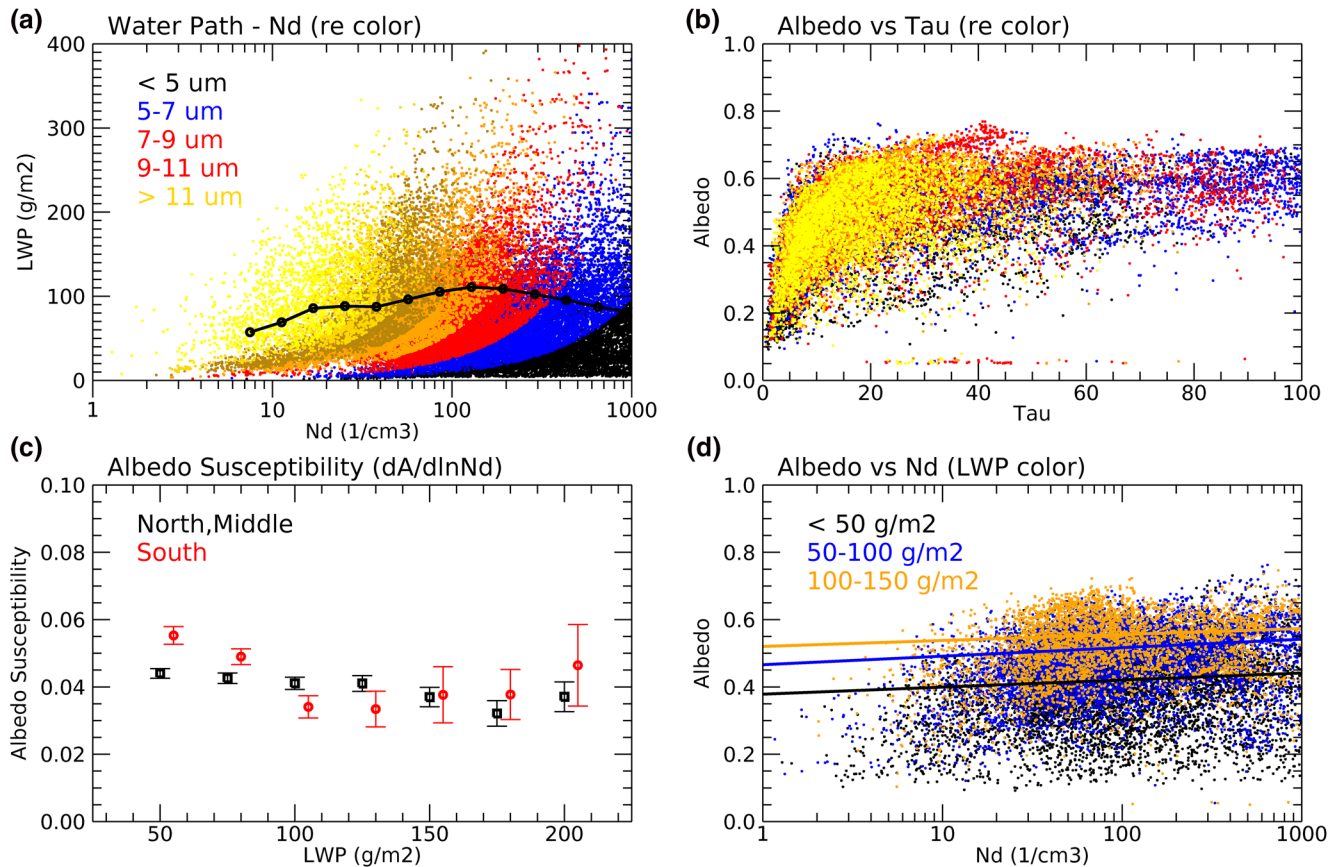
Figure 6. Derived cloud and radiation properties. (a) liquid water path as a function cloud droplet number concentration color coded by effective radius with black: sub 5 μm, blue: 5–7 μm, red: 7–9 μm, orange: 9–11 μm), yellow: >11 μm. The black curve with symbols show the mean LWP in cloud droplet number bins. (b) Albedo as function of optical depth with color coded re as in (a) (c) Albedo Susceptibility (dA/dln(Nd)). Red is the southern analysis domain. Black is the northern and middle domains. (d) Albedo as a function of N_d color coded for LWP with black < 50 g m^{-2}, blue denotes LWP from 50 to 100 g m^{-2}, and orange denotes LWP from 100 to 150 g m^{-2}. The lines denote linear regressions of albedo as a function of Nd in the LWP bins representing the albedo susceptibility as depicted in (c). LWP, liquid water paths.

function of both the amount of condensed water in the column and how that water is distributed into the DSD, the relationships are not necessarily straightforward. Often, microphysics derived from satellite radiometers use reflected sunlight to retrieve optical depth and r_e. The water path is then either derived from the optical depth and r_e or perhaps from combined microwave radiometer measurements. N_d is then further derived from assumptions. Our observations are of higher spatial resolution, and the microwave radiometer constrains the LWP. The lidar constrains the DSD's cross-sectional area, and the radar constrains the droplet sizes. While there are still significant uncertainties in the results, these unique measurements combined with simultaneous aerosol measurements allow us to explore the role that these clouds play in the SO atmosphere and surface energy balance.

Recently Gryspeerdt et al. (2019) examined global MODIS retrievals and found that cloud LWP is non monotonically related to N_d. LWP increased for lower N_d due to precipitation suppression, while at higher N_d, more rapid evaporation with smaller r_e seemed to cause water path to decrease with increasing N_d. Our data exclude precipitation. However, we do not control for the nearby presence of drizzle or snow. In other words, the nonprecipitating clouds we analyze could be associated with nearby precipitation and their properties modulated by precipitation processes. In Figure 6a, we plot the relationship of LWP as a function of Nd, and we color the scatter plot by r_e as described in the caption. LWP tends to increase with re for a given Nd. However, there seems to be some range (i.e., freedom) for LWP to vary for a given N_d-r_e pair. We note that this scatter plot is different from those shown in Gryspeerdt et al. (2019). However, by binning the LWP as a function of N_d and then plotting the median value of that LWP, we also find a relationship where LWP

tends to increase with N_d until about 100 cm^{-3} when the tendency is for LWP to begin decreasing with N_d. The inflection point in N_d that we find is larger than in Gryspeerdt et al. (2019) where the inflection point for oceanic clouds that include the Southern Ocean is approximately 60 cm^{-3} (their Figure 4b), but we can perhaps interpret the results similarly. Mace and Avey (2017) found similar effects on a seasonal basis using A-Train data, where a given precipitation rate required higher LWP at larger N_d found during the summer months.

While it seems that the DSD properties (r_e and N_d) can modulate the LWP through precipitation suppression, it is the LWP that largely controls the effect of the clouds on the energy budget. We illustrate this property in Figures 6b and 6d where we plot A as a function of N_d and visible optical depth with the LWP color-coded as in Figure 6a and r_e color-coded in Figure 6b. A increases with water path while the smaller r_e clouds tend to be associated with the higher optical depths and larger A. Simply linearly regressing A as a function of N_d in the LWP ranges for the common colored points in Figure 6b, we find that within a given LWP range, A tends to increase as N_d increases because increasing N_d is associated with decreasing r_e—although the primary factor in determining A remains the LWP. The slopes on these regression curves are the albedo susceptibility (Platnick & Twomey, 1994). Painemal and Minnis (2012) define the albedo susceptibility $S_R = dA/(d\ln N_d)$ where they use the linear regression slope A with N_d within LWP bins as in Figure 6b. We plot SR for the SO liquid phase clouds in Figure 6a. We find S_R values that are generally smaller than those found by Painemal and Minnins (2012) in the marine stratocumulus regions. Painemal and Minnins (2012) report maximum values of S_R that approach 0.09 in clouds that have overall lower LWP. Approximately 90% of our data have LWP greater than 20 g m^{-2} and less than 250 g m^{-2} with a mean value near 90 g m^{-2}. At its maximum near 0.045 (0.055 in the Southern region), the value of S_R implies that a doubling of N_d would result in about a 0.9% (1.1%) increase in A. Painemal and Minnins (2012) find a similar pattern although larger absolute values with a tendency for S_R to have a maximum at approximately 50 g m^{-2} and then decrease toward larger LWP. However, the decrease of S_R in the southern region is larger than in the more northern latitudes and reaches a minimum at lower LWP. We can understand the decrease of S_R with LWP by considering that a cloud layer's reflectance tends to asymptote to a maximum value as the optical depth increases beyond about 20. So, as the layer becomes optically thicker due to higher LWP, the ability for the microphysics to influence A lessens and thus, S_R decreases. These results suggest that the Southern latitude domain reaches this saturation point at smaller LWP, meaning that the cloud's A is less susceptible to microphysics overall. We can interpret this saturation of S_R at lower LWP in the southern domain to be due to lower effective radii and higher average N_d. The 95% confidence intervals in the regression slopes plotted on the figure show significant uncertainty, especially in the southern region at higher water paths. However, the systematic nature of the tendency of S_R with LWP provides confidence in the overall results.

4.3. Latitudinal Variations

Because the Southern Ocean's physical oceanography and seasonal biology influences cloud properties (i.e., Arloe et al., 2020; Armour et al., 2016; Deppeler & Davidson, 2017; Krüger & Graßl, 2011; D. T. McCoy et al., 2015), we take a closer look at the combined data set's latitudinal variability. We impose a convenient set of boundaries based on Deppler and Davidson (2017; Figure 2) that shows apparent variations in Chlorophyll-a in the longitudinal domain we consider. From Hobart's latitude to roughly 50°S, the ocean tends to have higher biological productivity and more quiescent weather during the summer months. The subAntarctic front near 50°S is the boundary between the subtropical waters to the north and the ACC and seasonal storm track. The Sub Antarctic Circumpolar Current Front's climatological position of 62.5°S at this longitude marks the entry into the Antarctic marginal seas. We will refer to these latitude bins as the northern (Hobart to 50°S), middle (50°S to 62.5°S), and southern (poleward of 62.5°S) analysis regions. Figure 7 summarizes the cloud and radiative properties of the nonprecipitating liquid clouds observed in these regions. Recall that the step increase in sulfate aerosol concentration and CCN and N_d in the 29 January case study (Figure 2) occurred near 64°S.

The LWP distribution (Figure 7a) shows the LWP decreasing overall toward the higher latitudes with a broader distribution in the southern analysis region. The Nd also has a clear progression except it is not monotonic with latitude with the middle region having the overall lowest N_d. The r_e shows that the three analysis domains all share a common modal peak near 9 μm while the northern and middle regions do tend
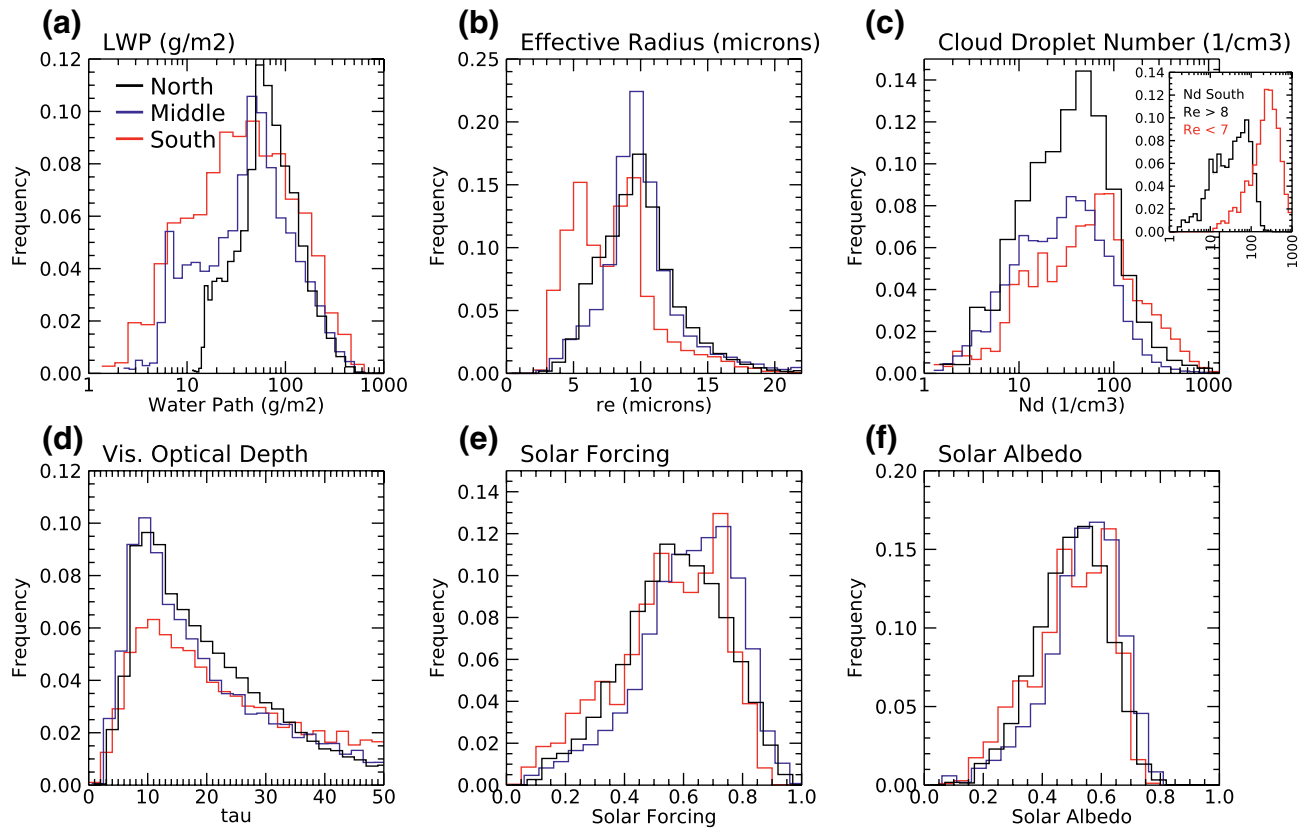
Figure 7. Latitudinal variations of retrieved cloud and derived radiative properties. Solid black denotes the northern analysis domain (Hobart to 50°S). Blue denotes the middle latitude domain (50°S–62.5°S). Red denotes the Southern Latitude domain (South of 62.5°S). See text for details. Panels a and c are additionally normalized by the bin width. The inset in panel c shows the N_d distributions for the Southern region when re is less than 7 μm (red) and greater than 8 μm (black).

to have a tail to larger values. In the southern region the r_e distribution is bimodal with a secondary peak near 5 μm.

Of interest is the bimodal nature of cloud and radiative properties in the southern analysis region. The inset in Figure 7c shows N_d for when r_e is in excess of 8 μm and less than 7 μm demonstrating that the two modes are clearly associated with distinct N_d modes. The January 29 case illustrates both droplet modes when sulfate aerosol concentrations and CCN increased, and cloud properties changed around 16 UTC. The bimodality in microphysics in the southern region translates to bimodality in the albedo as well (Figure 8f). We find one mode for the southern region near 0.45 similar to the albedo of regions to the north while another mode occurs at 0.65 due to the higher N_d clouds.

Figure 8 shows cloud and radiation properties compiled from 2–5 January 2018 when RSV Aurora Australis was at Casey Station near 66°S and 110°E. We show this case study to illustrate a prolonged period of high N_d clouds along the East Antarctic coast. There are 4050 30-s retrievals in these distributions. We plot the in-situ distributions for reference to show how much of a contrast these clouds presented to what was measured by the SOCRATES aircraft flights. The LWP during this event was higher than average, in the 200–300 g m^{-2} range, while the N_d was often more than 300 cm^{-3} with r_e around 5 μm. Comparing our calculation of the downwelling solar flux with the observations shows a distribution with a robust mode near zero difference with a skew toward positive values indicating a bias in the distribution's high N_d tail. However, with a solar noon clear sky flux near 800 W m^{-2}, the total solar forcing on this day was on the order of 500 W m^{-2}, suggesting that, on average, our estimates of the cloud microphysics were within the uncertainties discussed earlier. Thus, we find evidence for bimodality in cloud properties in the southern analysis domain, where one mode has the properties of marine clouds from farther north. In contrast, another mode has relatively high droplet numbers more consistent with high CCN air. The high LWP of
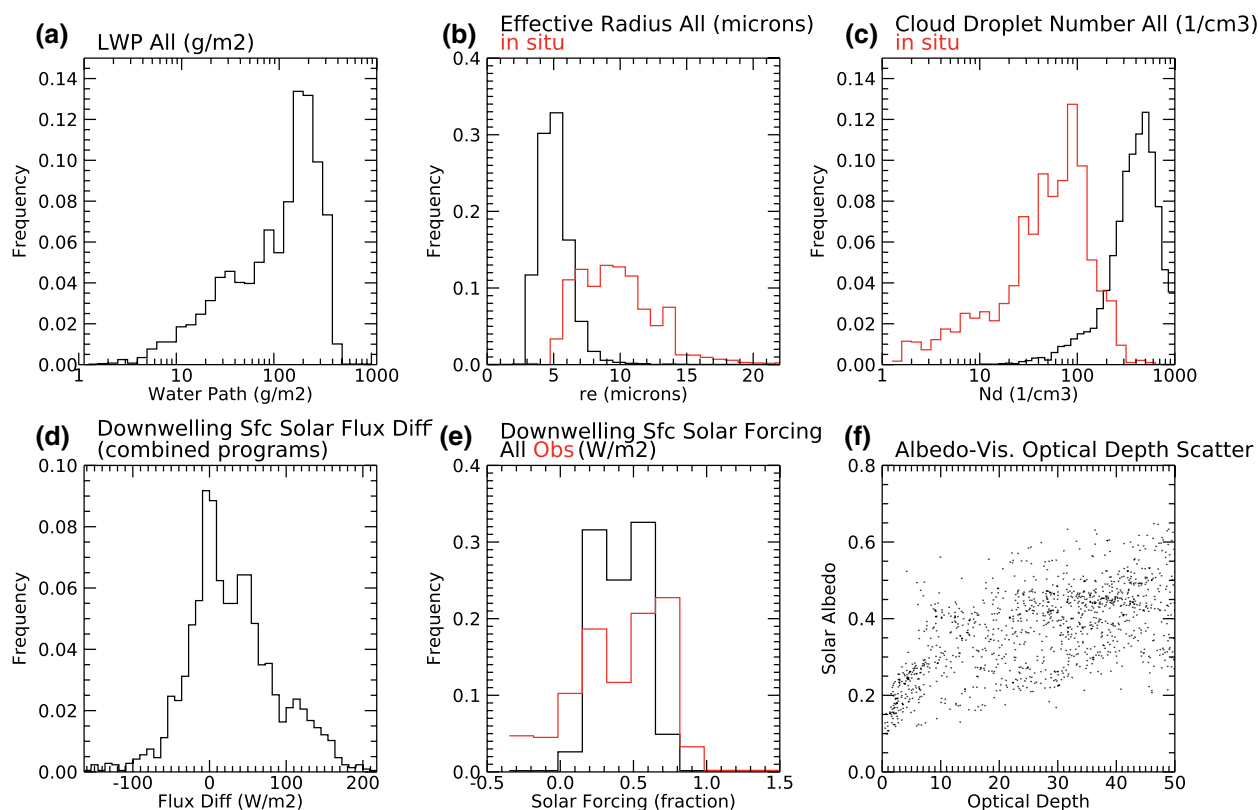
Figure 8. As in Figure 5 except for the 2–5 January 2018 MARCUS Case Study when the Aurora Australis was docked at Casey Station Antarctica. MARCUS, Measurements of Aerosols, Radiation and Clouds over the Southern Ocean.

these events implies the suppression of precipitation occurring in the high Nd droplet mode clouds. We also document a substantial effect on the albedo suggesting, if the high N_d clouds are derived from biogenic aerosol emissions, a feedback between the seasonal biology and the input of sunlight to the surface ocean.

The bimodality we find in cloud properties in the southern region raises the question of how those properties are distributed spatially. The transition we documented in our discussion of Figure 2 is just one of several rather abrupt transitions that we find in the data. In Table 2 we list all the transitions found during the MARCUS and CAPRICORN-II voyages. The 11 transitions we find are all south of the 62°S and nine of them are south of 65°S. The changes are toward both higher and lower N_d with the direction of change irrespective of the direction the ship was moving. Most of the transitions have a change in N_d of more than a factor of 3, and most of the transitions in N_d are accompanied by a similar change in CCN. An exception is the N_d transition from 100 to 50 cm^{-3} on 31 January and then a transition in the opposite direction a few hours later on 1 February. These transitions are bracketed by a period of light snow. It seems reasonable to question whether the occurrence of precipitation and perhaps scavenging of droplets by ice crystals is sufficient to reduce N_d.

We take these results to suggest that the bimodality we find in the southern analysis domain is often realized as distinct changes in air mass properties such as CCN and aerosol chemistry similar to the air mass changes described by Humphries et al. (2016) and in the case study in Figure 2. Additional study is needed to determine if the fine scale variability in aerosol chemistry that was observed during CAPRICORN II in this region can be traced to distinct air mass source regions.

4.4. Optical Depth-Temperature Response

As discussed recently in Terai et al. (2019; hereafter T19), there is a robust prediction among climate models that middle and high latitude clouds will contribute a negative feedback on the climate system

Table 2
Abrupt N_d Transition Cases

Date yyyy/mm/dd	Lat/Lon	Nd tendency (Approximate N_d change cm^{-3})	UTC time range	CCN tendency (Approximate CCN change cm^{-3})
Marcus N_d transitions				
November 12, 2017	65°S/80°E	High to Low (110–30)	10–15	60 cm^{-3} at 5 UTC no data afterward
November 24, 2017	62°S/95°E	Low to High (30–120)	1–4	Low to High (80–120)
December 31, 2017	66°S/110°E	High to Low (100–50)	5–10	No Data
January 6, 2018	63°S/114°E	Low to High (30–90)	7–8	Low to High (30–100)
February 18, 2018	67°S/70°E	Low to High (20–120)	7–8	Low to High (250–325)
February 18, 2018	67°S/70°E	High to Low (100–50)	11–12	High to Low (250–200)
February 19, 2018	69°S/78°E	Low to High (20–100)	2–5	Low to High (200–275)
CAPRICORN II N_d transitions				
Date yyyy/mm/dd	Lat/Lon	N_d tendency (Approximate N_d change cm^{-3})	UTC time range	CCN tendency (Approximate CCN change cm^{-3})
January 29, 2018	63°S/140°E	Low to High (50–100)	16–20	Low to High (130–265)
January 31, 2018	65°S/140°E	High to Low (100–50)	22–23	Steady at 250
February 1, 2018	66°S/141°E	Low to High (20–200)	1–3	Steady at 250
February 1, 2018	66°S/145°E	High to Low (200–90)	17–18	High to Low (250–200)

Abbreviation: CCN, cloud condensation nuclei.

Notes. For an event to be counted as a transition, we require a temporal change in N_d of at least a factor of two over a period of time not exceeding 5 h during which the retrievals were continuous.

because these clouds will increase in optical thickness with warming, thereby becoming more reflective. T19 comprehensively describes several possible physical mechanisms operating in middle latitude clouds that could cause them to either thicken or thin with warming (see also Gordon & Klein, 2014). These mechanisms include a phase feedback where ice precipitation would decrease in tendency, thereby causing clouds to have higher liquid water paths and longer lifetimes, a thickening because the moist adiabatic lapse rate steepens with warming (Betts & Harshvardan, 1987). Mechanisms that cause clouds to thin with increased temperature would occur due to more efficient cloud top drying. This drying could arise by decoupling of the boundary layer from the surface, allowing entrainment of dry, free tropospheric air to erode the cloud water path. All or most of these mechanisms are physically plausible and could work together or counter each other to form a net response. T19 examine ground-based measurements from several middle and high latitude sites and find that the mechanisms that cause overall thinning of clouds with warming are predominant. Huang et al. (2016) examine MODIS data over the SO and find a measurable decline in cloud optical depth with increasing SST due to a decrease in LWP associated with a decrease in cloud top height.

As shown in Figure 9, we find a negative trend of -0.62 K^{-1} in cloud optical depth with layer base temperature from the MARCUS and CAPRICORN data. While the correlation coefficient is weak at -0.18, the optical depth's tendency to decrease with temperature agrees with Huang et al. (2016) (-0.53 K^{-1}). T19 report their results in fractional units and find a value of -10% K^{-1} while our results in fractional units would be 4% K^{-1}. We find a margin of error at the 99% confidence level of 0.06 K^{-1} in the regression slope using a standard methodology (Giles & Klepinger, 1988). For verification, we randomly removed half of the ~70,000 measurements and recalculated the slope 1,000 times. The variability in the regression slopes reasonably replicated the confidence interval. We find that this regression line's slope implies a decrease in optical depth of approximately a factor 2 over the observations' temperature range (255–285 K). The scatter and resulting low correlation in this relationship is not unexpected, given the highly varied meteorology and differences in background aerosol over a seasonal cycle. That we see any coherent trend at all is notable. We examined the factors that influence the optical depth. We found no significant tendencies in r_e or N_d, but the LWP had a downward trend but with weaker statistical significance that seemed to be associated with
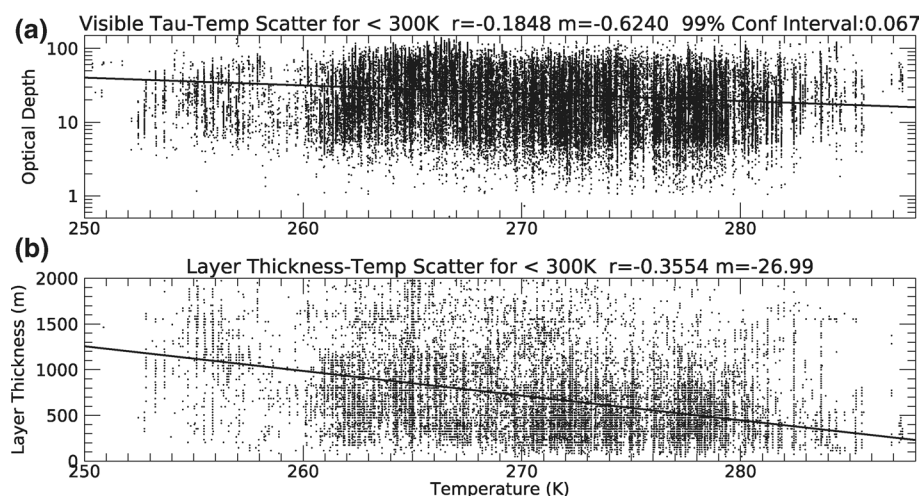
Figure 9. Regression of visible optical depth (a) and layer thickness (b) of the liquid phase non precipitating clouds as a function of layer base temperature for the combined CAPRICORN and MARCUS data sets. The titles show the linear correlation coefficient (r) and the physical slope of the regression line. For (a) m is the rate of change of optical depth per degree K. for (b) m is the rate of change of layer thickness in meters per degree K. CAPRICORN, Clouds Aerosols Precipitation Radiation and atmospheric Composition Over the SoutheRN ocean; MARCUS, Measurements of Aerosols, Radiation and Clouds over the Southern Ocean.

a decrease in cloud physical thickness (Figure 9b) over the temperature range considered. These results are consistent with the findings of Huang et al. (2016).

To further explore cloud properties′ sensitivity to thermal structure, we examine the radiosonde record compiled from the 2018 field missions. During CAPRICORN II and MARCUS, regular radiosonde soundings provide 410 soundings for analysis. Of these, 259 had marine inversions. We define a marine inversion as a potential temperature difference between the surface and 850 hPa layer (hereafter referred to as inversion strength) that exceeds 5 K. The median height of the marine inversion in this data set is 1.5 km. Of these, 76% (197) are decoupled using the method developed by Yin and Albrecht (2000) and as implemented in MP18a. While we find it difficult to draw robust conclusions from such a small number of soundings, the results provide context for the relationship between optical depth and temperature in Figure 9. Figure 10 summarize findings from the soundings. The conditions that allowed us to implement the retrieval algorithm were satisfied primarily when the marine boundary layer was decoupled; 190 decoupled soundings occurred within 1 h of a microphysical retrieval with 69 soundings for coupled conditions.

Overall, the decoupled boundary layers were colder and slightly cloudier with a mean inversion temperature of 265 K and cloud fraction of 72% versus 269 K and 65% for the coupled profiles. Inversion strengths were on average smaller in the decoupled profiles (6.1 K vs. 7.3 K). The data suggest that the mean LWP increases with inversion strength to approximately 10 K where the mean LWP asymptotes to ∼100 g m^{-2} (Figure 10a). However, the tendency in optical depth and cloud layer thickness shown in Figure 9 is not solely a function of whether or not the sounding was decoupled. In Figure 10b we plot the distribution of LWP for coupled and decoupled profiles and divide the decoupled into warm (inversion temperature >273 K) and cold (inversion temperature <273 K). The coupled LWP distribution is bimodal. The bimodality arises from open cellular cases where cumulus are often accompanied by stratocumulus (See MP18a for a case study). Note that the distribution of dBZ is also bimodal (Figure 10d). The LWP distribution in the decoupled conditions shows clear sensitivity to temperature suggesting that the warmer decoupled boundary layers have lower LWP on average.

The analysis of T19 suggests that decoupled boundary layers would tend to have lower water paths and occur in warmer temperatures. Our results in this middle latitude region suggest that while the LWPs do tend to be lower in decoupled conditions, they also tend to be colder than the coupled profiles. In decoupled
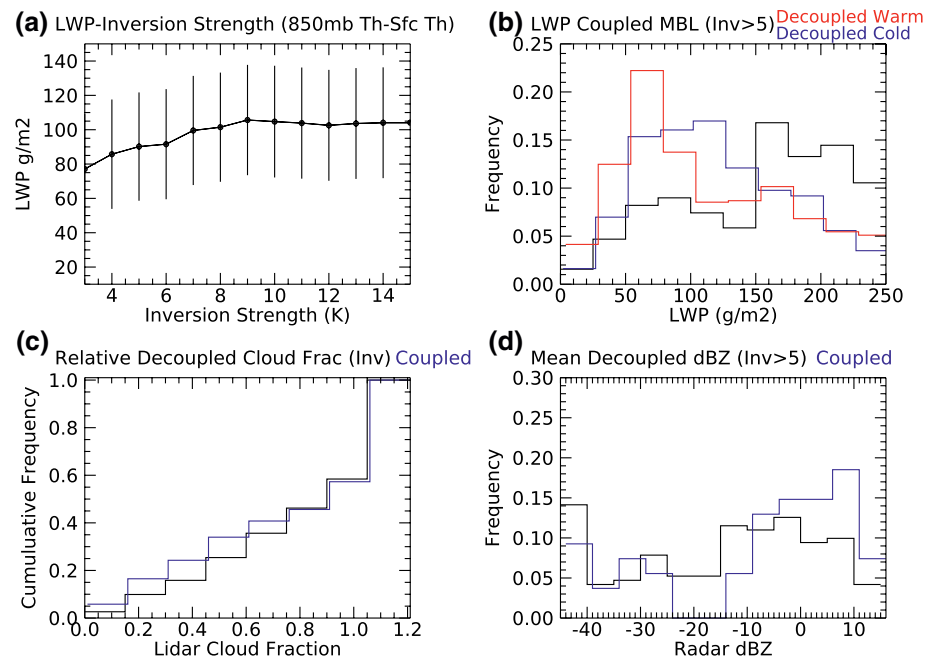
Figure 10. Statistics of soundings and coincident liquid water path retrievals (LWP) within 1 h of a sounding. (a) The mean and standard deviation of LWP as a function of inversion strength where inversion strength is defined as the potential temperature difference between the surface and 850 hPa. (b) LWP occurrence frequency for coupled and decoupled thermodynamic soundings. (c) cumulative distribution of lidar cloud fraction within 1.5 h of a sounding for coupled and decoupled profiles. (d) The frequency distribution of cloud-base cloud radar reflectivity for coupled and decoupled soundings.

conditions, the highest water paths are found in the coldest air with the strongest marine inversions. As the profile warms, the inversion weakens and the water paths tend to decrease. While it would take additional observations to develop robust statistics, the data are consistent with an evolution from open cell coupled profiles behind a cold front to the strongest marine inversions in the colder air near the surface high pressure ridge where the MBL is decoupled. The MBL, remaining decoupled, then transitions to weaker marine inversions and lower water paths in warmer air upstream of the surface ridge axis. This interpretation is consistent with the composite cyclone and cloud structures reported in Field and Wood (2007), Govekar et al., (2011), and Naud et al., (2016).

5. Summary and Conclusions

We have presented an analysis of data compiled over three ship-based field campaigns in the Southern Ocean between East Antarctica and Hobart, Tasmania. The data were collected aboard the Australian Research Vessels Investigator (CAPRICORN I and II) and RSV Aurora Australis (MARCUS). The MARCUS program ran during the summer resupply of the Casey, Davis, Mawson, and Macquarie Island stations between November 2017 and March 2018. The CAPRICORN II campaign took place in conjunction with the NSF-funded SOCRATES aircraft mission and was conducted over 6 weeks from early January 2018 until late February 2018. The CAPRICORN I campaign took place in March and April 2016 and was previously reported by Mace and Protat (2018a, 2018b).

We examine the properties of nonprecipitating liquid phase clouds. This cloud genre comprises nearly half of the MBL-based layers in the Southern Ocean between 40°S and 65°S based on an analysis of satellite radar and lidar data (Table 1). Combining the observations from the three measurement campaigns provides 480 h of measurements in these clouds. The critical measurements from the three campaigns that we use consist of the following zenith viewing measurements:

1. W-Band radar reflectivity
2. Elastic lidar attenuated backscatter, and
3. Zenith-viewing 31 GHz microwave brightness temperature

Together, these measurements allow us to constrain the LWP, effective radius (re), and cloud droplet number concentration N_d of the liquid non precipitating clouds using an optimal estimation algorithm that uses prior information from aircraft data collected during SOCRATES. Uncertainties in the retrieved quantities are within 20% for the LWP. N_d is much more difficult to constrain because it is the zeroth moment of the droplet size distribution, while the measurements tend to constrain higher-order moments. Uncertainties in r_e and N_d are typically 10% and 70% depending on whether the clouds have measurable radar reflectivity since the nonprecipitating clouds often fall below the radars' detection thresholds (~25% of the time during CAPRICORN and 12% of the time during Marcus). In such circumstances, the uncertainties in r_e rise to 50% and N_d to 120%.

Overall, the nonprecipitating clouds that we examine over the summertime SO tend to have LWP between 100 and 200 g m^{-2}, r_e of 8.7 μm and N_d near 90 cm^{-3} on average, making the clouds somewhat thicker with smaller r_e and higher N_d than their counterparts in the subtropical stratocumulus regions. The clouds have visible optical depths between 20 and 30 with a mean of 27 and the clouds remove approximately ½ of the surface downwelling solar flux. Albedos are typically near 0.5.

The SO clouds are similar in many ways to eastern ocean basin stratocumulus clouds with subtle differences. For instance, we find that higher N_d clouds in the Southern Ocean tend to be associated with higher LWP values up to N_d of ~110 cm^{-3} beyond which the mean water paths tend to decrease. Gryspeerdt et al. (2019) associate this behavior with suppression of precipitation—a process that Mace and Avey (2017) documented in SO clouds between summer and winter using A-Train satellite data. We also find that the tendency for albedo to be modulated by N_d is somewhat smaller for the nonprecipitating clouds over the SO than for similar clouds in the eastern subtropical oceans because the clouds are optically thicker. We do find that the albedo susceptibility decreases as the LWP increases to about 200 g m^{-2} in agreement with other studies (Painemal & Minnins, 2012) of subtropical stratocumulus. The clouds over the SO also tend to have an optical depth response to temperature change that is similar to findings reported from Northern Hemisphere ground sites by Terai et al. (2019) and for SO clouds analyzed from satellite by Huang et al. (2016) where the clouds tend to decrease in optical depth with temperature by about 4% per Kelvin. While there is considerable scatter in this relationship due to the underlying natural variability, these results have reasonable statistical significance. They seem to be due to a thinning of the geometrical cloud layer thickness with temperature.

Perhaps most significantly, we find a bimodality in cloud properties along the coast of East Antarctica with one cloud property mode exhibiting properties consistent with the maritime clouds observed farther north. The other mode has smaller r_e and is associated with larger N_d that, through precipitation suppression, allows for higher LWP to be maintained along with a concurrent increase in albedo and surface solar forcing. We document a transition between these regimes with a case study from CAPRICORN II on January 29, 2018 when cloud r_e and N_d simultaneously decreased and increased over the space of ~30 min. A step-change in the aerosol sulfate concentrations and CCN measured at the surface occurred 1 h after the increase in N_d. We found no compositional markers for continental aerosol, suggesting that these were pristine marine air masses not altered by land emissions. The nonprecipitating clouds retained the smaller r_e and higher N_d properties for several days while the aerosol number concentrations remained mostly elevated. We also demonstrate another case at Casey station of very high N_d and small r_e clouds that persisted over several days. We identified 11 cases of abrupt transitions in N_d in the southern analysis region during the CAPRICORN II and MARCUS campaigns with nine of them exhibiting similar trends in CCN. While additional study is needed, this variability is consistent with distinct air mass changes along the East-Antarctic marginal ice zone associated with air that contains significantly different aerosol characteristics. Such variability in aerosol has been documented in previous field data by Humphries et al., (2016) and more recently by Alroe et al., (2020).

This work raises many questions regarding the properties and processes that modulate cloudiness in the Southern Ocean. That we see such remarkable sensitivity of this cloud genre to changes in the background

aerosol suggests that there is much to learn regarding the aerosol-cloud-precipitation interactions in this region. The much higher albedo in the enhanced N_d clouds, if associated with the emission of sulfate aerosol of biogenic origin, imply a strong feedback between the seasonal biology and the sunlight input to the high latitude Southern Ocean. From a climatological standpoint, these results also raise questions about biogenic aerosol's role in modulating the seasonal aerosol background state of the entire SO (Mace & Avey, 2017; D. T. McCoy et al., 2015). To what extent is the increase in summertime N_d over the wider SO caused by the large biological phytoplankton blooms concentrated along the marginal seas of Antarctica (Shaw, 1987)? Is there a general increase in biogenic aerosol throughout the broader SO? Our data are limited by bracketing the summer season. For instance, what happens during fall as the biogenic emissions subside? When during spring do biogenic aerosol sources begin to impact cloud and precipitation properties? Is this transition related to biogeochemical cycling of sulfur compounds in melting sea ice (Damm et al., 2016)? The Southern Ocean is undergoing substantial changes with climate change (Armour et al., 2016; Kennicut et al., 2014; Liu et al., 2018) and understanding the implications of these changes require documentation and understanding of the processes occurring in the high latitude circumpolar Southern Ocean.

Data Availability Statement

All data used in this study are available in public archives. MARCUS data are available from the DOE ARM archive at https://adc.arm.gov/armlogin/login.jsp, SOCRATES data are available at https://data.eol.ucar.edu/project/SOCRATES, CAPRICORN I and II data are available at https://doi.org/10.25919/5f688fcc97166.

References

Abel, S. J., Walters, D. N., & Allen, G. (2010). Evaluation of stratocumulus cloud prediction in the Met Office forecast model during VOCALW-REx. *Atmospheric Chemistry and Physics*, *10*, 10541–10559. https://doi.org/10.5194/acp-10-10541-2010

Alexander, S. P., & Protat, A. (2018). Southern Ocean cloud properties as observed from the surface and satellite. *Journal of Geophysical Research: Atmospheres*, *123*, 443–456. https://doi.org/10.1002/2017JD026552

Alexander, S. P., & Protat, A. (2019). Vertical profiling of aerosols with a combined Raman- elastic backscatter lidar in the remote Southern Ocean marine boundary layer (43–66°S,132–150°E). *Journal of Geophysical Research: Atmospheres*, *124*(22), 12107–12125. https://doi.org/10.1029/2019JD030628

Alroe, J., Cravigan, L. T., Miljevic, B., Johnson, G. R., Selleck, P., Humphries, R. S., et al.(2020). Marine productivity and synoptic meteorology drive summer-time variability in Southern Ocean aerosols. *Atmospheric Chemistry and Physics*, *20*, 8047–8062. https://doi.org/10.5194/acp-20-8047-2020

Armour, K. C., Marshall, J., Scott, J. R., Donohoe, A., & Newsom, E. R. (2016). Southern Ocean warming delayed by circumpolar upwelling and equatorward transport. *Nature Geoscience*, *9*, 549–554. https://doi.org/10.1038/NGEO2731

Ayers, G. P., & Gras, J. L. (1991). Seasonal relationship between cloud condensation nuclei and aerosol methanesulphonate in marine air. *Nature*, *353*, 834–835.

Berry, E., Mace, G. G., & Gettelman, A. (2019). Using A-Train observations to evaluate cloud occurrence and radiative effects in the Community Atmosphere Model during the Southeast Asia summer monsoon. *Journal of Climate*, *32*, 4145–4165. https://doi.org/10.1175/JCLI-D-18-0693.1

Berry, E., Mace, G. G., & Gettelman, A. (2020). Using A-Train observations to evaluate East Pacific cloud occurrence and radiative effect in the Community Atmosphere Model. *Journal of Climate*, *32*, 4145–4165. https://doi.org/10.1175/JCLI-D-19-870.1

Betts, A. K., & Harshvardhan (1987). Thermodynamic constraint on the cloud liquid water feedback in climate models. *Journal of Geophysical Research*, *92*, 8483–8485.

Bodas-Salcedo, A., Hill, P., Furtado, K., Williams, K., Field, P., Manners, J., et al. (2016). Large contribution of supercooled liquid clouds to the solar radiation budget of the Southern Ocean. *Journal of Climate*, *29*, 4213–4228. https://doi.org/10.1175/JCLI-D-15-0564.1

Bodas-Salcedo, A., Mulcahy, J. P., Andrews, T., Williams, K. D., Ringer, M. A., Field, P. R., & Elsaesser, G. S. (2019). Strong dependence of atmospheric feedbacks on mixed-phase microphysics and aerosol-cloud interactions in HadGEM3. *Journal of Advances in Modeling Earth Systems*, *11*, 1735–1758. https://doi.org/10.1029/2019MS001688

Bodas-Salcedo, A., Williams, K. D., Field, P. R., & Lock, A. P. (2012). The surface downwelling solar radiation surplus over the Southern Ocean in the Met Office Model: The role of midlatitude cyclone clouds. *Journal of Climate*, *25*, 7467–2498.

Bodas-Salcedo, A., Williams, K. D., Ringer, M. A., Beau, I., Cole, J. N. S., Dufresne, J. –L., et al. (2014). Origins, of the solar radiation biases over the Southern Ocean in CFMIP2 Models. *Journal of Climate*, *27*, 41–57. https://doi.org/10.1175/JCLI-D-13-00169.1

Damm, E., Nomura, D., Martin, A., Dieckmann, G. S., & Meiners, K. M. (2016). DMSP and DMS cycling within Antarctic sea ice during the winter-spring transition. *Deep-Sea Research II*, *131*, 150–159. http://dx.doi.org/10.1016.j.dsr2.2015.12.015

Delanoë, J., Protat, A., Vinson, J.-P., Brett, W., Caudoux, C., Bertrand, F., et al. (2016). BASTA, a 95 GHz FMCW Doppler radar for cloud and fog studies. *Journal of Atmospheric and Oceanic Technology*, *33*, 1023–1038.

Deppeler, S. L., & Davidson, A. T. (2017). Southern Ocean phytoplankton in a changing climate. *Frontiers in Marine Science*, *4*, 40. https://doi.org/10.3389/fmars.2017.00040

Field, P. R., & Wood, R. (2007). Precipitation and cloud structure in midlatitude cyclones. *Journal of Climate*, *20*, 233–254. https://doi.org/10.1175/JCLI3998.1

Fossum, K. N., Ovadnevaite, J., Ceburnis, D., Dall'Osto, M., Marullo, S., Bellaicco, M., et al. (2018). Summertime primary and secondary contributions to Southern Ocean cloud condensation nuclei. *Scientific Reports*, *8*, 13844. https://doi.org/10.1038/s41598-018-32047-4

Frey, W. R., & Kay, J. E. (2017). The influence of extratropical cloud phase and amount feedbacks on climate sensitivity. *Climate Dynamics*, *50*, 3097–3116. https://doi.org/10.1007/s00382-017-3796-5

Fröhlich, R., Cubison, M. J., Slowik, J. G., Bukowiecki, N., Prévôt, A. S. H., Baltensperger, U., et al. (2013). The ToF-ACSM: A portable aerosol chemical speciation monitor with TOFMS detection. *Atmospheric Measurement Techniques*, *6*, 3225–3241. https://doi.org/10.5194/amt-6-3225-2013

Gettelman, A., Bardeen, C. G., McCluskey, C. S., Jarvinen, E., Stith, J., & Bretherton, C. (2020). Simulating observations of Southern Ocean clouds and implications for climate. *Journal of Geophysical Research: Atmospheres*, *125*, e2020JD032619. https://doi.org/10.1029/2020JD032619

Giles, E., & Klepinger, L. (1988). Confidence intervals for estimates based on linear regression in forensic anthropology. *Journal of Forensic Sciences*, *33*(5), 1218–1222. https://doi.org/10.1520/JFS12555J

Gordon, N. D., & Klein, S. A. (2014). Low-cloud optical depth feedback in climate models. *Journal of Geophysical Research: Atmospheres*, *119*, 6052–6065. https://doi.org/10.1002/2013JD021052

Govekar, P. D. C., Jakob, M. J., & Reeder, J. H. (2011). The three-dimensional distribution of clouds around Southern Hemisphere extratropical cyclone. *Geophysical Research Letters*, *38*, L21805. https://doi.org/10.1029/2011GL049091

Gryspeerdt, E., Goren, T., Sourdeval, O., Quaas, J., Mulmenstadt, J., Dipu, S., et al. (2019). Constraining the aerosol influence on cloud liquid water path. *Atmospheric Chemistry and Physics*, *19*, 5331–5347. https://doi.org/10.5194/acp-19-5331-2019

Huang, Y., Siems, S. T., Manton, M. J., Rosenfeld, D., Marchand, R., McFarquhar, G. M., & Protat, A. (2016). What is the role of sea surface temperature in modulating cloud and precipitation properties over the Southern Ocean? *Journal of Climate*, *29*, 7453–7473. https://doi.org/10.1175/JCLI-D-15-0768.1

Hu, Y., Winker, D., Vaughan, M., Lin, B., Omar, A., Trepte, C., et al. (2009). CALIPSO/CALIOP cloud phase discrimination algorithm. *Journal of Atmospheric and Oceanic Technology*, *26*, 2293–2309. https://doi.org/10.1175/2009JTECHA1280.1

Humphries, R. S., Klekociuk, A. R., Schofield, R., Keywood, M., Ward, J., & Wilson, S. R. (2016). Unexpectedly high ultrafine aerosol concentration above East Antarctic sea ice. *Atmospheric Chemistry and Physics*, *16*, 2185–2206. https://doi.org/10.5192/acp-16-2185-2016

Kato, S., Smith, G. L., & Barker, H. W. (2001). Gamma-weighted discrete ordinate two-stream approximation for computation of domain-averaged solar irradiance. *Journal of the Atmospheric Sciences*, *58*, 3797–3803.

Kay, J. E., Wall, C., Yettella, V., MedeirosHannay, B. C., Caldwell, P., & Bitz, C. (2016). Global climate impacts of fixing the Southern Ocean shortwave radiation bias in the Community Earth System Model. *Journal of Climate*, *29*, 4617–4636. https://doi.org/10.1175/JCLI-D-15-0358.1

Kelleher, M. K., & Grise, K. M. (2019). Examining Southern Ocean cloud controlling factors on daily time scales and their connections to midlatitude weather systems. *Journal of Climate*, *32*, 5145–5159. https://doi.org/10.1175/JCLI-D-18-0840.1

Kennicutt, M. C., II, Chown, S. L., Cassano, J. J., Liggett, D., Peck, L. S., et al. (2014). A roadmap for Antarctic and Southern Ocean science for the next two decades and beyond. *Antarctic Science*, *27*(1), 3–18.

Kirk, P. D. W., & Stumpf, M. P. H. (2009). Gaussian process regression bootstrapping: Exploring the effects of uncertainty in time course data. *Bioinformatics*, *25*, 1300–1306.

Klein, S. A., Hall, A., Norris, J. R., & Pincus, R. (2017). Low-Cloud feedbacks from cloud-controlling factors: A review. *Surveys in Geophysics*, *38*, 1307–1329. https://doi.org/10.1007/s10712-017-9433-3

Klepp, C., Michel, S., Protat, A., Burdanowitz, J., Albern, N., Dahl, A., et al. (2018). OceanRAIN, a new in-situ shipboard global ocean surface-reference dataset of all water cycle components. *Nature–Scientific Data*, *5*, 180122. https://doi.org/10.1038/sdata.2018.122

Kollias, P., Treserras, B. P., & Protat, A. (2019). Calibration of the 2007-2017 record of ARM cloud radar observations using CloudSat. *Atmospheric Measurement Techniques*, *12*, 4949–4964. https://doi.org/10.5194/amt-12-4949-2019

Krüger, O., & Graßl, H. (2011). Southern Ocean phytoplankton increases cloud albedo and reduces precipitation. *Geophysical Research Letters*, *38*, L08809. https://doi.org/10.1029/2011GL047116

Li, J. Y. Hu, Huang, J., Stamnes, K., Yi, Y., & Stamnes, S. (2011). A new method for retrieval of the extinction coefficient of water clouds by using the tail of the CALIOP signal. *Atmospheric Chemistry and Physics*, *11*, 2903–2916. https://doi.org/10.5194/acp-11-2903-2011

Liljegren, J., Clouthiaux, E. E., Mace, G. G., Kato, S., & Dong, X. (2001). A new retrieval for cloud liquid water path using a ground-based microwave radiometer and measurements of cloud temperature. *Journal of Geophysical Research*, *106*(D14), 14485–14500.

Liu, W. J., Lu, J., Xie, S.-P., & Fedorov, A. (2018). Southern Ocean heat uptake, redistribution and storage in a warming climate: The role of meridional overturning circulation. *Journal of Climate*, *31*, 4727–4743. https://doi.org/10.1175/JCLI-D-17-07061.1

Lu, M.-L., Sorooshian, A., Jonsson, H. H., Feingold, G., Flagan, R. C., & Seinfeld, J. H. (2009). Marine stratocumulus aerosol-cloud relationships in the MASE II experiment: Precipitation susceptibility in Eastern Pacific marine stratocumulus. *Journal of Geophysical Research*, *114*, D24203. https://doi.org/10.1029/2009JD012774

Maahn, M., Turner, D. D., Lohnert, U., Posselt, D. J., Kerstin, E., Mace, G. G., & Comstock, J. M. (2020). Optimal estimation retrievals and their uncertainties: What every atmospheric scientist should know. *Bulletin of the American Meteorological Society*, *101*(9), E1512–E1523. https://doi.org/10.1175/BAMS-D-19-0027.1

Mace, G. G., & Avey, S. (2017). Seasonal variability of warm boundary layer clouds and precipitation properties in the Southern Ocean as diagnosed from A-Train data. *Journal of Geophysical Research: Atmospheres*, *122*, 1015–1032. https://doi.org/10.1002/2016JD025348

Mace, G. G., Avey, S., Cooper, S., Lebsock, M., Tanelli, S., & Dobrowalski, G. (2016). Retrieving co-occurring cloud and precipitation properties of warm marine boundary layer clouds with A-Train data. *Journal of Geophysical Research: Atmospheres*, *120*, 4008–4033. https://doi.org/10.1002/:2015JDO23681

Mace, G. G., Benson, S., & Hu, Y. (2020). On the frequency of the occurrence of the ice phase in supercooled Southern Ocean low clouds derived from CALIPSOI and CloudSat. *Geophysical Research Letters*, *47*, e2020GL087554. https://doi.org/10.1029/2020GL087554

Mace, G. G., & Protat, A. (2018a). Clouds of the the Southern Ocean from the RV Investigator during CAPRICORN. Part 2: The properties of non precipitating stratocumulus. *Journal of Applied Meteorology and Climatology*, *57*, 1805–1823. https://doi.org/10.1175/JAMC-D-17-0195.1

Mace, G. G., & Protat, A. (2018b). Clouds over the Southern Ocean from the RV Investigator during CAPRICORN. Part 1: Cloud occurrence and phase partitioning. *Journal of Applied Meteorology and Climatology*, *57*, 1783–1803. https://doi.org/10.1175/JAMC-D-17-0194.1

Mace, G. G., & Zhang (2014). The Cloudsat Radar-Lidar Geometrical Profile Algorithm (RL-GeoProf): Updates, improvements, and selected results. *Journal of Geophysical Research: Atmospheres*, *119*(15), 9441. https://doi.org/10.1002/2013JD021374

Marchand, R., Mace, G. G., Ackerman, T., & Stephens, G. (2008). Hydrometeor detection using CloudSat—An Earth-orbiting 94-GHz cloud radar. *Journal of Atmospheric and Oceanic Technology*, *25*, 519–533. https://doi.org/10.1175/2007JTECHA1006.1

McCoy, D. T., Burrows, S. M., Wood, R., Grosvenor, D. P., Elliott, S. M., Ma, P., et al. (2015). Natural aerosols explain seasonal and spatial patterns of Southern Ocean cloud albedo. *Science Advances*, *1*, e1500157.

McCoy, D. T., Field, P. R., Elsaesser, G. S., Bodas-Salcedo, A., Kahn, B. H., Zelinka, M. D., et al. (2019). Cloud feedbacks in extratropical cyclones: Insights from long-term satellite data and high resolution global simulations. *Atmospheric Chemistry and Physics*, *19*, 1147–1172. https://doi.org/10.5194/acp-19-1147-2019

McCoy, I. L., McCoy, D. T., Wood, R., Regayre, L., Watson-Parris, D., Grosvenor, D. P., et al. (2020). The hemispheric contrast in cloud microphysical properties constrains aerosol forcing. *Proceedings of the National Academy of Sciences*, *117*(32), 18998–19006. https://doi.org/10.1073/pnas.1922502117

McFarquhar, G., Bretherton, C., Marchand, R., Protat, A., DeMott, P., Alexander, S., et al. (2020). Unique observations of clouds, aerosols, precipitation, and surface radiation over the Southern Ocean: An overview of CAPRICORN, MARCUS, MICRE, and SOCRATES. *Bulletin of the American Meteorological Society*. https://doi.org/10.1175/BAMS-D-20-0132.1

Naud, C. M., Booth, J. F., & Del Genio, A. D. (2016). The relationship between boundary layer stability and cloud cover in the post-cold-frontal region. *Journal of Climate*, *29*, 8129–8149. https://doi.org/10.1175/JCLI-D-15-0700.1

O'Connor, E. J., Illingworth, A. J., & Hogan, R. J. (2004). A technique for autocalibration of cloud lidar. *Journal of Atmospheric and Oceanic Technology*, *21*, 777–786.

O'Dowd, C. D., Lowe, J. A., & Smith, M. H. (1997). Biogenic sulphur emissions and inferred non-sea-salt-sulphate cloud condensation nuclei in and around Antarctica. *Journal of Geophysical Research*, *102*, 12839–12854.

Painemal, D., & Minnins, P. (2012). On the dependence of albedo on cloud microphysics over marine stratocumulus clouds regimes determined from Clouds and the Earth's Radiant Energy System (CERES) data. *Journal of Geophysical Research*, *117*, D06203. https://doi.org/10.1029/2011JD017120

Platnick, S., & Twomey, S. (1994). Determining the susceptibility of cloud albedo to changes in droplet concentration with Advanced Very High Resolution Radiometer. *Journal of Applied Meteorology*, *33*, 334–347.

Platt, C. M. R., Winker, D. M., Vaughan, M. A., & Miller, S. D. (1999). Backscatter-to-extinction ratios in the top layers of tropical mesoscale convective systems and in isolated cirrus from LITE observations. *Journal of Applied Meteorology*, *38*, 1330–1345.

Posselt, D., & Mace, G. (2014). The influence of parameter uncertainty on snowfall retrievals using Markov Chain Monte Carlo solution methods. *Journal of Applied Meteorology and Climatology*, *53*, 2034–2057.

Protat, A., Bouniol, D., O'Connor, E. J., Baltink, H. K., Verlinde, J., & Widener, K. (2011). CloudSat as a Global Radar Calibrator. *Journal of Atmospheric and Oceanic Technology*, *28*, 445–452.

Protat, A., Schulz, E., Rikus, L., Sun, Z., & Xiao, Y. (2017). Shipborne observations of the radiative effect of Southern Ocean Clouds. *Journal of Geophysical Research: Atmospheres*, *122*, 318–328.

Rauber, R. M., et al. (2006). Rain in shallow cumulus over the ocean; the RICO campaign. *Bulletin of the American Meteorological Society*, *87*, 1912–1919.

Rodgers, C. D. (2000). *Inverse methods for atmospheric sounding, theory and practice*. Singapore: World Scientific Publishing Co. Ltd..

Royer, P., Bizard, A., Sauvage, L., & Thobois, L. (2014). *Validation protocol and intercomparison campaigns with the R-MAN510 aerosol lidar*. Paper presented at the Proceedings of the 17th International Symposium for the Advancement of Boundary-Layer Remote Sensing, ISARS, Auckland, New Zealand.

Savic-Jovcic, V., & Stevens, B. (2008). The structure and mesoscale organization of precipitating stratocumulus. *Journal of the Atmospheric Sciences*, *65*, 1587–1605.

Schulz, E. W., A Josey, S., & Verein, R. (2012). First air-sea flux mooring measurements in the Southern Ocean. *Geophysical Research Letters*, *39*, L16606. https://doi.org/10.1029/2012GL052290

Shaw, G. E. (1988). Antarctic Aerosols: A Review. *Reviews of Geophysics*, *26*(1), 89–112.

Stephens, G. L., Vane, D. G., Tanelli, S., Im, E., Durden, S., Rokey, M., et al. (2008). CloudSat mission: Performance and early science after the first year of operation. *Journal of Geophysical Research*, *113*, D00A18. https://doi.org/10.1029/2008JD009982

Tanelli, S., Durden, S. L., Im, E., Pak, K. S., Reinke, D. G., Partain, P., et al. (2008). CloudSat's Cloud Profiling Radar after two years in orbit: Performance, calibration, and processing. *IEEE Transactions on Geoscience and Remote Sensing*, *46*, 3650–3663. https://doi.org/10.1109/TGRS.2008.2002030

Tan, I., Storelvmo, T., & Zelinka, M. D. (2016). Observational constraints on mixed phase clouse imply higher climate sensitivity. *Science*, *352*, 224–228. https://doi.org/10.1126/science.aad5300

Terai, C. R., Zhang, Y., Klein, S. A., Zelinka, M. D., Chiu, J. C., & Min, Q. (2019). Mechanisms behind the extratropical stratiform low-cloud optical depth response to temperature in ARM site observations. *Journal of Geophysical Research: Atmospheres*, *124*, 2127–2147. https://doi.org/10.1029/2018JD029359

Toon, O. B., McCay, C. P., Ackerman, T. P., & Santhanam, K. (1989). Rapid calculation of radiative heating rate and photodissociation rates in inhomogeneous multiple scattering atmospheres. *Journal of Geophysical Research*, *94*, 16287–16301.

Trenberth, K. E., & Fasullo, J. T. (2010). Simulation of present-day and twenty-first-century energy budgets of the Southern Oceans. *Journal of Climate*, *23*, 440–454. https://doi.org/10.1175/2009JCLI3152.1

Twomey, S. (1977). The influence of pollution o the shortwave albedo of clouds. *Journal of the Atmospheric Sciences*, *34*, 1149–1152.

Vergara-Temprado, J., Miltenberger, A. K., Furtado, K., Grosveno, D. P., Shipway, B. J., Hill, A. A., et al. (2018). Strong control of Southern Ocean cloud reflectivity by ice nucleating particles. *Proceedings of the National Academy of Sciences*, *115*(11), 2687. https://doi.org/10.1073/pnas.1721627115

Wall, C. J., Hartmann, D. L., & Ma, P.-L. (2017). Instantaneous linkages between clouds and large-scale meteorology over the Southern Ocean in observations and a climate model. *Journal of Climate*, *30*, 9455–9474. https://doi.org/10.1175/JCLI-D-17-0156.1

Wang, Y., McFarquhar, G. M., Rauber, R. M., Zhao, C., Wu, W., Finlon, J. A., et al. (2020). Microphysical properties of generating cells over the Southern Ocean: Results from SOCRATES. *Journal of Geophysical Research: Atmospheres*, *125*(13). https://doi.org/10.1029/2019JD032237

Winker, D. M., Vaughan, M. A., Omar, A., Hu, Y., Powell, K., Liu, Z., et al. (2009). Overview of the CALIPSO mission and CALIOP data processing algorithms. *Journal of Atmospheric and Oceanic Technology*, *26*, 2310–2324. https://doi.org/10.1175/2009JtechA1281.1

Yin, B., & Albrecht, B. A. (2000). Spatial variability of atmospheric boundary layer structure over the eastern equatorial Pacific. *Journal of Climate*, *13*, 1574–1592. https://doi.org/10.1175/1520-0442(2000)013,1574:SVOABL.2.0.CO;2